Remote Sensing of Environment 251 (2020) 112083

Contents lists available at ScienceDirect

Remote Sensing of Environment

journal homepage: www.elsevier.com/locate/rse

Comparison of total emitted solar-induced chlorophyll fluorescence (SIF) and top-of-canopy (TOC) SIF in estimating photosynthesis

Xiaoliang Lu[a], Zhunqiao Liu[a,b], Feng Zhao[c], Jianwu Tang[b,*]

[a] State Key Laboratory of Soil Erosion and Dryland Farming on the Loess Plateau, Institute of Soil and Water Conservation, Northwest A&F University, Yangling, Shaanxi 712100, China
[b] The Ecosystems Center, Marine Biological Laboratory, Woods Hole, MA 02543, USA
[c] School of Instrumentation Science and Opto-Electronics Engineering, Beijing University of Aeronautics and Astronautics, Beijing 100191, China

ARTICLE INFO

Keywords:
Solar-induced fluorescence
Gross primary production
Fluorescence escape ratio
Top-of-canopy SIF
Total emitted SIF and the recollision theory

ABSTRACT

Many studies have shown that solar-induced fluorescence (SIF) has a good potential to predict gross primary production (GPP) of vegetation. What we measured by remote sensing or near-surface platforms is top-of-canopy (TOC) SIF (SIF_{toc}), which is not necessarily equal or proportional to total emitted SIF (SIF_{tot}) from the entire canopy due to the (re)absorption and scattering effects. However, photosynthesis, the process that plants use to fix carbon from the atmosphere, occurs at the entire vertical canopy. Here, by using the recollision theory, we calculated SIF_{tot} at 760 nm from the measured SIF_{toc}, hyperspectral reflectance (R), canopy interception (i) and leaf albedo (ω_l). Among them, both SIF_{toc} and R can be obtained from concurrent TOC spectral measurements; i and ω_l in the near-infrared region can be estimated from the open access datasets with a good accuracy. Our result confirms that the measured SIF_{toc} only accounts for a small fraction of SIF_{tot}: the above-the-canopy sensor can only "see" on average 22.9% of SIF_{tot} at Harvard Forest. SIF_{tot} has the following advantages over SIF_{toc} in estimating GPP: (1) SIF_{tot} improves the diurnal estimate of canopy GPP, especially capable to capture the midday depression of photosynthesis which may cause the large discrepancies between SIF_{toc} and GPP on a diurnal basis, (2) SIF_{tot} produces a stronger correlation with GPP from plants with complex canopy structure or under sky conditions with more diffuse irradiance, and (3) the SIF_{tot}-GPP relationship shows a stronger resilience to environmental stresses. The fluorescence escape ratio (f_{esc}), the ratio between SIF_{toc} multiplied by π and SIF_{tot}, is mostly determined by the sun-canopy-sensor geometry and leaf inclination distribution. The effect of LAI and the leaf chlorophyll concentration on f_{esc} is marginal at the 760 nm wavelength. Our results suggest that converting SIF_{toc} into SIF_{tot} provides a better tool to understand and estimate GPP.

1. Introduction

Photosynthesis is one of the most important processes in the Earth by which green plants converts CO_2 in the atmosphere, and water and inorganic nutrients in soils into organic compounds and O_2. During this process, absorbed solar energy has three pathways including energy consumed in photosynthesis, heat loss, and chlorophyll fluorescence emissions at longer wavelengths or called solar-induced chlorophyll fluorescence (SIF). SIF is sourced from two photosystems named Photosystems I and II (PS I and PS II, Porcar-Castell et al., 2014): SIF from Photosystem I is mainly in the near-infrared (NIR) range (> 700 nm) with one peak at around 740 nm; SIF emitted from Photosystem II covers almost the complete SIF spectrum from 640 to 850 nm with two peaks at about 685 and 740 nm, respectively. Because SIF emissions are part of the photosynthesis process, many recent studies have reported that SIF is closely linked to photosynthesis activities. For example, Frankenberg et al. (2011) found a strong correlation between the global annual SIF retrieved from the Greenhouse Gases Observing Satellite (GOSAT) and gross primary productivity (GPP) extrapolated from the Max Planck Institute for Biogeochemistry (MPI-BGC) model. Guanter et al. (2014) showed that SIF observations from Global Ozone Monitoring Instrument 2 (GOME-2) compared well with estimates of GPP at both site and large continuous spatial levels. Yang et al. (2015) and Yang et al., 2017a found that ground-based measurements of SIF emission had a good performance in predicting plant photosynthesis from leaf to canopy scales.

GPP is produced from all the leaves in the canopy, while top-of-canopy (TOC) SIF (SIF_{toc}) observed with a given field of view by ground-based, airborne or spaceborne sensor is only a portion of total emitted SIF from the entire canopy (SIF_{tot}), reflecting partial GPP

* Corresponding author.
E-mail address: jtang@mbl.edu (J. Tang).

https://doi.org/10.1016/j.rse.2020.112083
Received 25 September 2019; Received in revised form 10 August 2020; Accepted 6 September 2020
Available online 28 September 2020

mostly occurred on top of the canopy. Thus, SIF_{toc} may produce a poor correlation with GPP for ecosystems with a dense canopy. Furthermore, vegetation canopy structure plays an important role in regulating canopy leaving SIF signals. For example, Liu et al. (2016) reported that SIF_{toc} of winter wheat was closely related to leaf area index (LAI), orientation of leaves and viewing directions. Van Wittenberghe et al. (2015) found that leaf structure had a strong impact on bidirectional SIF emission properties in the NIR domain. A model-based study (Verrelst et al., 2015) also showed that large part of the variability in SIF_{toc} was related to variations in LAI and leaf angle distribution (LAD). All these findings suggest that the ignorance of effects of leaf optical properties and canopy structure on the behaviors of the radiative transfer of SIF in canopy may cause large uncertainties in interpreting relationships between SIF_{toc} and plant photosynthetic activity.

Because of the discrepancy of SIF_{toc} and SIF_{tot}, many efforts have been made to reduce variations in SIF-GPP correlations caused by vegetation canopy structure and varying sun-canopy-sensor geometry. For example, SIF observations with normalizing solar zenith angle are found to have stronger correlations with GPP (Frankenberg et al., 2011; Joiner et al., 2011). Liu et al. (2016) corrected directional variations in SIF by using a modified bidirectional reflectance distribution function model. He et al. (2017) developed a geometric-optical bidirectional reflectance model to correct the impact of angular of SIF observation and they showed that angular normalized SIF observations had a better performance to predict GPP than original SIF observations. Alternatively, SIF_{toc} may be downscaled to either leaf or photosystem level. By considering the absorption and scattering of SIF emission within the canopy, SIF_{toc} may be downscaled to total emitted fluorescence by all leaves. Moreover, it can be further downscaled to total emitted fluorescence by all photosystems if the absorption process within the leaf is also accounted for. Retrieval of SIF signals emitted from the whole canopy is important to estimate canopy GPP: total emitted fluorescence at either leaf or photosystem level better represents SIF emission integrated over all the leaves within the canopy which may be more comparable to photosynthetic activity. For example, Liu et al. (2019) downscaled SIF_{toc} to the photosystem level by using the Random Forest (RF) model and showed that SIF emitted from photosystems produced a stronger relationship with absorbed photosynthetically active radiation (APAR). However, its performance depended on *selecting inputs for the RF model and* the representativeness of the training datasets.

The similarity between the bidirectional SIF emission and reflectance (Liu et al., 2016) suggests that directional reflectance may have a good potential to express the scattering/(re)absorption processes of SIF signals travel through vegetation canopy. For instance, Yang and van der Tol (2018) showed that canopy scattering of SIF emission in the NIR domain can be represented by TOC reflectance. In this study, by using the concept of recollision probability to describe the radiative transfer of SIF emission within the canopy (Smolander and Stenberg, 2005; Stenberg et al., 2016), we first expressed the leaf level SIF emission (SIF_{tot}) at 760 nm from measurements of SIF_{toc} and directional reflectance factor (R). We also examined the effect of leaf pigments and canopy structure on the variations of the fluorescence escape ratio (f_{esc}) of SIF at 760 nm which is defined as the ratio between SIF_{toc} multiplied by π and SIF_{tot} (i.e. $SIF_{toc} \times \pi/SIF_{tot}$). We then evaluated the performance of SIF_{tot} in estimating canopy GPP at the forest research site. The impacts of LAI, ratio of diffuse irradiance, radiation saturation, the illumination geometry and the meteorological variables on the SIF_{tot}-GPP relationship were also analyzed.

2. Materials and methods

2.1. Study site and measurements

Our study site is located at the Harvard Forest, Petersham, Massachusetts, USA (42°32′07.2″N 72°11′23.4″W). The dominant forest types are American beech (*Fagus grandifolia Ehrh*), red oak (*Quercus rubra*) and red maple (*Acer rubrum* L). The mean stand age is about 80 years and forest height is around 20 m. At the Harvard forest, carbon and water fluxes are continuously measured at the Environmental Measurement Station (EMS). We acquired hourly GPP for the EMS tower in 2014 from Long-Term Ecological Research (LTER) website. The canopy photosynthetically active radiation (PAR, μmol m^{-2} s^{-1}) and the fraction of diffuse PAR were obtained by the quantum sensor (PQS-1, Kipp & Zonen B.V., Delft, Netherlands) at the EMS tower. The other meteorological variables used in this study including air temperature (T_{air}, °C), air pressure (P, hPa), wind speed (u, ms^{-1}), atmospheric vapor pressure (ea, hPa) and atmospheric CO_2 concentration (C_a, ppm) were measured at the 30-m meteorology tower which is about 1.4 km from the SIF measurement site.

The SIF observation system located on the walk-up tower has started to measure canopy-level SIF emission from 2013 (Yang et al., 2015). The main components of the SIF system are: one spectrometer (HR2000+, OceanOptics, Inc., Dunedin, Florida) and two fiber optics. The spectrometer has a spectral resolution of 0.13 nm for the spectral region from 680 nm to 775 nm. One optic points upward to collect incident irradiance (E, W m^{-2} nm^{-1}) and other points downward to the forest to collect up-welling radiance (L, W m^{-2} sr^{-1} nm^{-1}). The sensor collected irradiance/radiance every 5 s. In 5 min intervals, the system provided one irradiance measurement and the average of 59 canopy radiance measurements. The dark current correction was also implemented for every measurement. We used the Spectral Fitting Method (SFM) (Meroni et al., 2010; Zhao et al., 2014) to retrieve both R and SIF_{toc} from irradiance/radiance (see Section 3.4). The system is installed 5 m above the top of canopy and the viewing zenith angle is 30 degree ($\theta_v = 30°$) to avoid the obstruction due to the tower (Yang et al., 2015). All observations had an angular FOV of 25° which made its footprint cover a round with the diameter of 5 m at the top of canopy (Fig. 1). In 2014 when we collected data for this study, irradiance/radiance were measured from early May to late October at a 5-min time step (Yang et al., 2017a). Since we focus on SIF and R at 760 nm and the direction of observation is fixed, we will not explicitly include λ and Ω_o in the following text unless they are needed otherwise.

We used the destructive method (Yang et al., 2017b) to measure the leaf chlorophyll concentrations (C_{ab}, ug cm^{-2}) and carotenoid content (C_{car}, ug cm^{-2}) weekly in spring (DOY (day of year) 133–167) and autumn (DOY 261–301), and biweekly in summer (DOY 261–301) in 2014. At each filed work, 12 leaves were sampled from the upper canopy and leaf discs were then punched from leaves. Chlorophyll and carotenoid were extracted by frozen leaf discs in a cold mortal using acetone/MgO mixture. After centrifugation, a spectrophotometer (Shimazu UV-1201, Kyoto, Japan) was then used to measure the absorbance of the supernatant at 470, 645 and 662 nm. C_{ab} and C_{car} were estimated from the absorption spectrum. Also at each field work, more leaves were collected to calculate dry matter content (C_{dm}, mg cm^{-2}) and leaf water thickness (C_{w}, mm). More information in estimating these variables can be found in Yang et al. (2017b). We also measured LAI values at a daily time step during spring and autumn and bi-weekly intervals during the growing season. The C_{ab}, C_{car}, C_{dm}, C_{w} and LAI time series were linearly interpolated into a daily time step for the next analysis.

2.2. Calculation of the total emitted SIF (SIF_{tot})

Yang and van der Tol (2018) showed that f_{esc}, the fluorescence escape ratio (Mohammed et al., 2019), can be expressed as:

$$f_{\mathrm{esc}} = \frac{R}{i \times \omega_l} \tag{1}$$

where R is the directional reflectance factor, i is canopy *interceptance, and* ω_l is leaf albedo. Note that Yang and van der Tol only considered the condition for direct sunlight as the TOC light source in developing Eq. (1). In practical applications, however, both the direct sunlight and diffuse skylight are present.

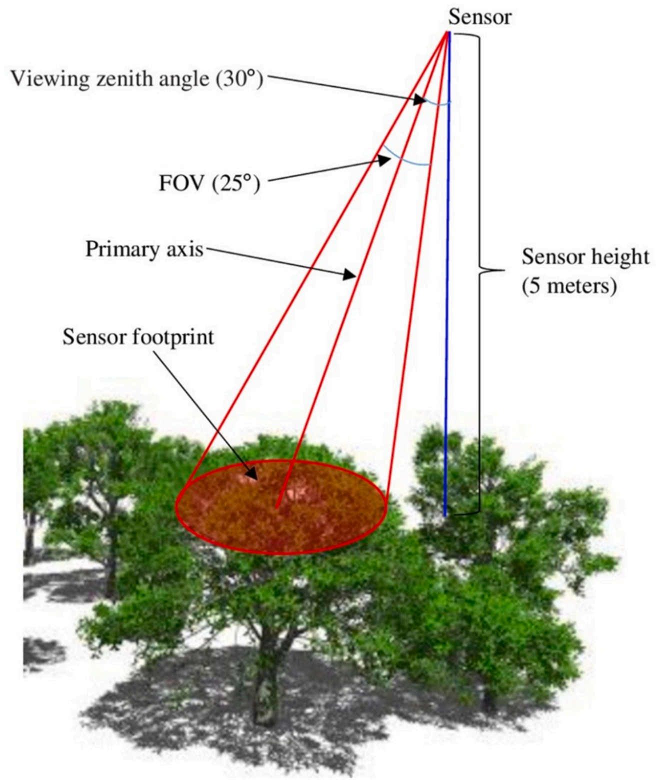

Fig. 1. Directional SIF emission at 760 nm (SIF_{toc}, mW m^{-2} sr^{-1} nm^{-1}) measured by the sensor at a height of 5 m above top of forest canopy. The view of zenith and field of view (FOV) of the sensor is 30° and 25°, respectively. The light red region represents the sensor's footprint (m^2) on the top of forest canopy. (For interpretation of the references to colour in this figure legend, the reader is referred to the web version of this article.)

In this study, we used the Monte Carlo ray-tracing based Weighted Photon Spread (WPS, Zhao et al., 2015) model and the method proposed by Yang et al. (2017c) to show that Eq. (1) still holds with a good accuracy when both direct sunlight and diffuse skylight are present at TOC (see Appendix and supplementary information). Accordingly, the canopy interceptance (i) is obtained by combining the interceptance of direct and diffuse solar radiation:

$$i = i_s \times (1 - f_d) + i_d \times f_d \tag{2}$$

where i_s and i_d represent the canopy interceptance for direct and diffuse solar irradiance, respectively; f_d is the fraction of diffuse solar irradiance at TOC; i_s is wavelength independent and depends on direction of solar beam and canopy structure. By using the Beer-Lambert law of light extinction (Monsi and Saeki, 2005), i_s for a canopy is expressed as:

$$i_s = 1 - e^{-CI*\mathrm{LAI}*\mathrm{G}(\theta_s)/\cos\theta_s} \tag{3}$$

where C_I is a clumping index (Chen and Black, 1992); θ_s is solar zenith angle (SZA); $\mathrm{G}(\theta_s)$ is the projection of a unit leaf area onto the surface normal to the direction of beam and is determined by the distribution of leaf inclination angles (see below). i_d can be expressed as (Stenberg, 2007):

$$i_d = 1 - 2 \times \int_0^{\pi/2} e^{-CI\times\mathrm{LAI}\times\mathrm{G}(\theta_s)/\cos\theta_s} \times \cos\theta_s \times \sin\theta_s d\theta_s \tag{4}$$

Similarly, the relationship between SIF_{tot} and SIF_{toc} can be extended to a more general condition in real near surface remote sensing with the presence of both the direct sunlight and diffuse skylight (see Appendix):

$$SIF_{tot} = \frac{\pi \times SIF_{toc} \times i \times \omega_l}{R} \tag{5}$$

SIF_{tot} is leaf total emitted fluorescence flux density free of (re)absorption, in unit of mW m^{-2} nm^{-1}, while SIF_{toc} is SIF signal measured by the sensor, in unit of mW m^{-2} sr^{-1} nm^{-1}. Both R and SIF_{toc} can be obtained from measurements of irradiance and radiance provided by a spectrometer (see below). ω_l varies at different wavelengths and is a function of leaf biophysical and structural properties.

From Eqs. (2), (3) and (4), f_d, C_I and $\mathrm{G}(\theta_s)$ should be determined to estimate i. We assumed that f_d can be represented by the fraction of diffuse PAR. Previous studies (Chen et al., 2005; Leblanc et al., 2005) showed that C_I value is linearly correlated with normalized difference between normalized hotspot and darkspot (NDHD) index. To estimate NDHD index, a bidirectional reflectance distribution function (BRDF) model should be selected to describe surface anisotropic features. However, different BRDF models may yield considerably different NDHD results (Maignan et al., 2004). By evaluating a variety of BRDF models, Wei and Fang (2016) used the best NDHD configuration to produce the global 500 m 8-day C_I maps from MODIS BRDF parameter data (MCD43A1) (Schaaf et al., 2002). These C_I maps are provided at National Earth System Science Data Sharing infrastructure (http://www.geodata.cn), we exacted the 8-day C_I time series in 2014 and interpolated it into a daily time step.

Leaf inclination distribution should be defined to calculate the G-function (Wang et al., 2007). We selected the distribution function proposed by Verhoef (1998) to describe proportion of leaf inclination angles at the study site. Although we did not measure leaf inclination angle in this study, another study (Raabe et al., 2015) which was also conducted at the Harvard Forest in 2015 showed that the leaf inclination angle distribution was plagiophile in the spring but remained planophile during the rest of the growing season. Note that LAD is mainly decided by species type and phenological stage. Considering that there was no large difference in the climate conditions between 2014 and 2015, it is reasonable to use the same LAD in this study. Accordingly, LIDFa and LIDFb, two parameters defining LAD (Wang et al., 2007), were assumed to be 0 and − 1 in the spring and they were set as 1 and 0 in the rest of the study period (Verhoef, 1998).

2.3. Estimation of ω_l

We used the PROSPECT model (Feret et al., 2008) to simulate ω_l at the study site. PROSPECT considers the impacts of leaf biochemical and leaf structural properties on the leaves reflectance and transmittance within the spectral range of 400–2500 nm. These properties were assigned actual measurements whenever available, otherwise their default values were used. The interpolated daily C_{ab}, C_{car}, C_{dm} and C_w (Fig. S1) were used in the PROSPECT simulation (Section 3.1); the rest two properties including senescent material (C_s, fraction) and anthocyanins content (C_{ant}, ug cm^{-2}) were kept fixed at their default values. PROSPECT uses the leaf structure parameter (N) to account for the impact of the mesophyll structure on leaf optical properties. We assumed that N remained relatively constant and It ($N = 1.7$) was equal to the ratio of reflectance and transmittance of the leaves measured at the study site in 2012 (Yang et al., 2016).

2.4. Estimation of R and SIF_{toc}

The up-welling radiance received by the sensor contains two coupled contributions: one is from reflected solar irradiance and the other is from SIF emission. However, it is only possible to distinguish from each other at absorption lines in the atmosphere or at spectral bands where solar irradiance is significantly low (Fraunhofer lines) (Meroni et al., 2009). In this study, we retrieved SIF emission using SFM at the

O_2-A absorption line within the spectral range of 757.00–771.00 nm. Around the absorption line (λ_{ab}), both R and SIF_{toc} can be expressed by the Taylor polynomials (Zhao et al., 2014):

$$R(\lambda_{ab}) = b_0 + b_1 * (\lambda_{ab} - \lambda_{cab}) + b_2 * (\lambda_{ab} - \lambda_{cab})^2 \tag{6}$$

$$\mathrm{SIF}_{toc}(\lambda_{ab}) = b_3 + b_4 * (\lambda_{ab} - \lambda_{cab}) + b_5 * (\lambda_{ab} - \lambda_{cab})^2 \tag{7}$$

$$\lambda_{ab} \in (757\text{–}771 \text{ nm})$$

where b_0,b_1, b_2, b_3, b_4 and b_5 are six unknown coefficients in the above two equations; λ_{cab}, the central wavelength of the O_2-A absorption line, was set as 761 nm in this study. At the sensor, TOC radiance (L, W m^{-2} sr^{-1} nm^{-1}) contains contribution from both fluorescence and reflected solar energy:

$$L(\lambda_{ab}) = \mathrm{SIF}_{toc}(\lambda_{ab}) + \frac{E(\lambda_{ab}) * R(\lambda_{ab})}{\pi} \tag{8}$$

where E (W m^{-2} nm^{-1}) represents *down-welling solar irradiance*. By substituting Eq. (6) and (7) into Eq. (8), we have:

$$L(\lambda_{ab}) = (\lambda_{ab} - \lambda_{cab})^2 * \frac{E(\lambda_{ab})}{\pi} * b_2 + (\lambda_{ab} - \lambda_{cab}) * \frac{E(\lambda_{ab})}{\pi} * b_1 + \frac{E(\lambda_{ab})}{\pi} * b_0 + b_3 + b_4 * (\lambda_{ab} - \lambda_{cab}) + b_5 * (\lambda_{ab} - \lambda_{cab})^2 \tag{9}$$

To determine the unknown six coefficients in Eq. (9), one should have at least six measurements within the O_2-A absorption region. The sensor which has a spectral resolution of 0.13 nm provided samples much more than six within the O_2-A absorption line and the least squares method was used to retrieve the above six coefficients. We excluded measurements with poor fitting performance for Eq. (9) ($R^2 < 0.99$) from the further analysis (Yang et al., 2015).

After determining the coefficients in Eq. (9), we can estimate instantaneous R and SIF_{toc} at 760 nm with Eq. (6) and (7). Because measurement of incident light may contain more uncertainties in the first hours after sunrise and the hours before sunset, we only used R and SIF_{toc} acquired between 9 a.m. and 4 p.m. local time. Instantaneous R and SIF_{toc} were averaged into hourly scales. Either R or SIF_{toc} may have abnormal variations due to moving clouds and winds (alter the LAD). The smooth filter with a 3-h window was used to remove outliers of hourly SIF_{toc} (beyond/below 100% of the local average) and we finally obtained 984 hourly observations.

3. Results

After showing several key time series at the study site in 2014, we evaluated the temporal variation in SIF_{toc}, SIF_{tot}, and f_{esc}, and the performance of SIF_{toc} and SIF_{tot} in predicting GPP using linear regression. The impacts of LAI, the illumination conditions, the sun-canopy-sensor geometry and the environmental factors were then analyzed. All the regression coefficients are significant ($p < 0.05$). The coefficient of determination (R^2) and root mean square error (RMSE) were used to quantify the accuracy of the regression models.

3.1. Time series

The time series of daily LAI and C_I are shown in Fig. 2a. LAI rose rapidly in the spring and early summer which increased from 0.8 to 3.9 between DOY 128 and 170 (Fig. 2a); LAI values showed small variations during the maturity period in June, July and early August (Fig. 2a). Leaves started to drop in the late of August and LAI values decreased with a much faster rate from the middle of September which reached a minimum at 0.55 on DOY 312 (Fig. 2a). In contrast, the C_I time series generally kept stable at around 0.6 during the period of DOY 128 and 314 (Fig. 2a). The C_I values showed a slight increase trend when LAI values were relatively low: they increased to about 0.7 in the early spring and late autumn seasons (Fig. 2a).

The time series of i and ω_l are plotted with an hourly time step (Fig. 2b). The seasonal variation of i generally followed the phenological stages of LAI changes: its values increased rapidly from about 0.26 to more than 0.8 from the early spring to the end of May; they remained more than 0.9 during the most time of the summer season and they decreased from about 0.8 to 0.3 during October. The time series of i also contained stronger short-term variations (Fig. 2b), showing that i is also the function of solar zenith angle (Eq. (4)). In contrast, ω_l demonstrated a much more stable trend during the whole study period (Fig. 2b): it remained almost constant at around 0.88 (Fig. 2b).

Daily SIF_{toc}, R, SIF_{tot} and f_{esc} during the daytime (9 a.m. and 4 p.m. local time) and their standard deviations across the season are plotted in Fig. 3. The appearance of missing values, for example a gap period in the early summer, were mostly owing to the power failure. The time series of SIF_{toc} contained the obvious phenological transitions (Fig. 3a): it increased in the spring as the photosynthetic activity increased; it remained around 1 mW m^{-2} sr^{-1} nm^{-1} with moderate variations in the summer and it began to decrease in the early autumn. By contrast, R had a much smaller temporal variability: it increased rapidly in the early spring and maintained a long period of the summer plateau with the average of around 0.19 (Fig. 3b). Note that canopy-level reflectance is typically lower than that at the leaf level due to contribution from woody component in forest canopy. SIF_{tot} also showed a similar phenological trend to SIF_{toc} (Fig. 3c): it changed rapidly in both spring development and autumn senescence; its values varied between 8 mW m^{-2} nm^{-1} and 16 mW m^{-2} nm^{-1} during most of the summer time. f_{esc} had strong fluctuations during the whole study period and it had no obvious phenological changes (Fig. 3d). Its values varied in the range between 0.09 and 0.66 with a mean of 0.229, indicating that the sensor only received on average 22.9% of total emitted SIF. Although the model-based result (Yang and van der Tol, 2018) showed that the scattering of total emitted SIF increased with LAI, our result showed variations in LAI had no dominating impact on f_{esc} in the NIR region.

The mean diurnal courses of SIF_{toc}, GPP, SIF_{tot} and f_{esc} were also calculated from the hourly datasets in 2014 (Fig. 4). To make Fig. 4, we only used the days which had valid values for all these four variables during the whole period from 9 a.m. to 4 p.m. All of them showed the clear diurnal patterns: they had low values at the hours of the early morning and late afternoon and high values around midday (Fig. 4). However, SIF_{toc} did not exactly track the diurnal shapes of the SIF_{tot} and GPP: SIF_{toc} had the steeper morning increase and afternoon decline with a peak at 12:00 p.m. (Fig. 4a), while GPP had a less variation around noon (Fig. 4b). In contrast, SIF_{tot} better reproduced the diurnal course of GPP: both remained relatively stable between 11:00 a.m. and 2:00 p.m. (Fig. 4 b,c). Although f_{esc} did not contain a clear seasonal trend (Fig. 3d), it had a similar diurnal pattern to SIF_{toc}: both had their maximum values at noon (Fig. 4 a,d). Further, f_{esc} showed a more asymmetric pattern: it showed an increasing trend in the morning hours, but it had higher values and remained more stable in the afternoon.

3.2. The performance of SIF_{toc} and SIF_{tot} in estimating GPP

Fig. 5 provides the correlation coefficient (R^2) and root-mean-square error (RMSE) between GPP and SIF_{toc} and SIF_{tot} at an hourly and daily time step. Overall, SIF_{tot} had a better performance than SIF_{toc} in predicting GPP at an hourly scale: SIF_{toc} and SIF_{tot} accounted for 50.9% (RMSE = 0.30 g C m^{-2} h^{-1}, Fig. 5a) and 63.6% (RMSE = 0.25 g C m^{-2} h^{-1}, Fig. 5b) of variance in hourly GPP, respectively. The daily time step further enhanced the performance of both SIF_{toc} and SIF_{tot}. However, the longer time step tended to reduce the predictive

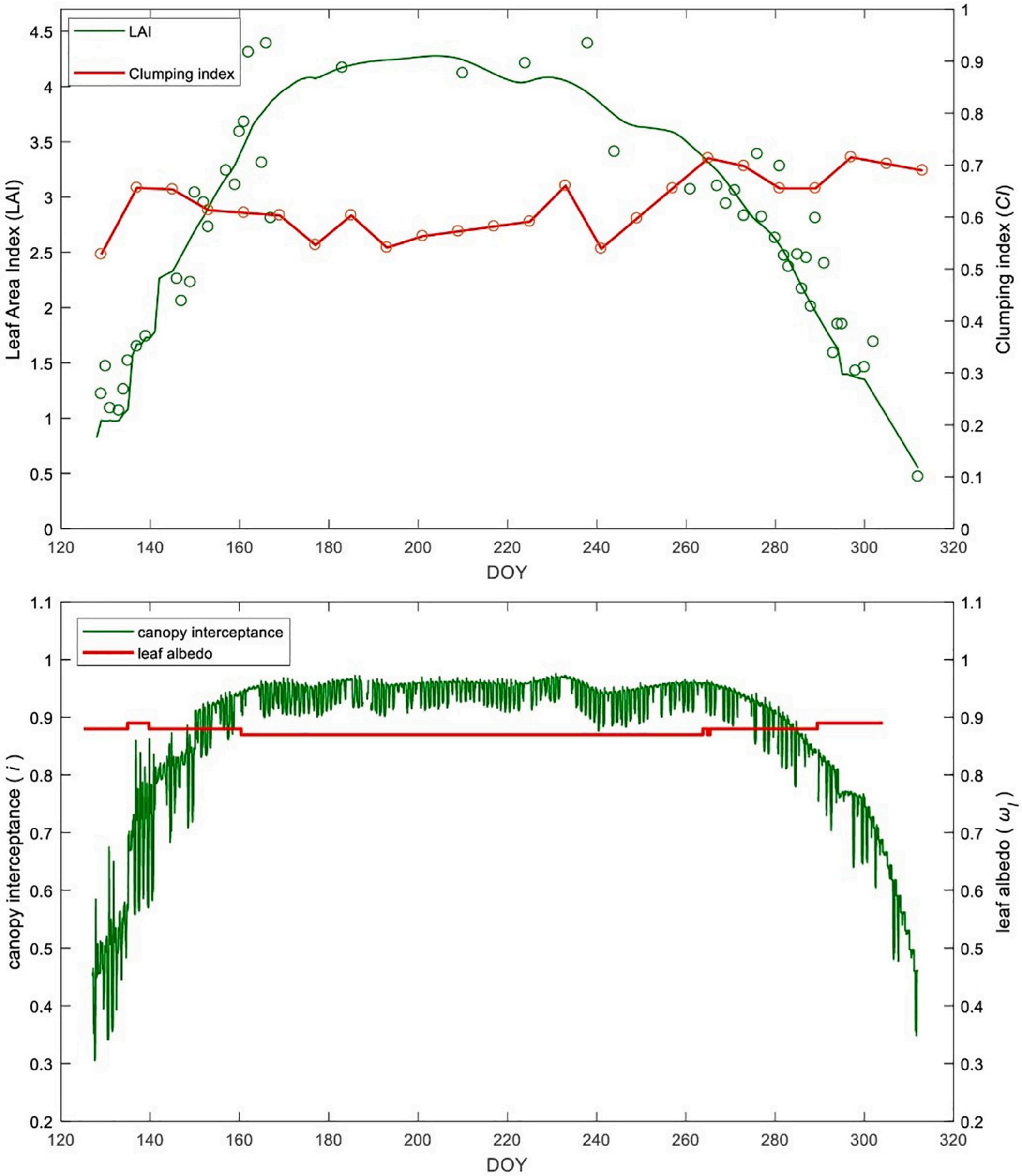

Fig. 2. Time series of daily (a) leaf area index (LAI $m^2\ m^{-2}$) and (a) clumping index (C_I), the markers to indicate the filed measurements; time series of hourly (b) canopy interception (i) and (b) leaf albedo (ω_l) at the study site in 2014. i was not estimated when solar zenith angle was higher than 85°.

advantage of SIF_{tot}: SIF_{toc} determined 66.1% (RMSE = 1.90 g C m^{-2} day^{-1}, Fig. 5c) of the variability in the daily GPP time series, whereas SIF_{tot} produced the modest improvement by explaining 71.4% (RMSE = 1.72 g C m^{-2} day^{-1}, Fig. 5d).

One important assumption in deriving Eq. (5) is that the contribution of soil reflectance is negligible. Also, the main motivation to use SIF_{tot} is to improve the correlation between SIF signals and GPP for dense canopies. Therefore, it is necessary to investigate how LAI affects the relationships between GPP and these two SIF-related variables. In order to do so, we separated hourly SIF (SIF_{toc} and SIF_{tot}) and GPP into three groups according to LAI values: (1) low: LAI ≤ 2.0, (2) medium: 2.0 < LAI ≤ 3.5 and (3) high: LAI ≥ 3.5.

LAI had a complex impact on the relationship between SIF emission and GPP (Table 1). SIF_{toc} governed 46.5% (RMSE = 0.21 g C m^{-2} h^{-1}) of variability in hourly GPP when LAI is medium, while the correlations between SIF_{toc} and GPP deteriorated under either low or high LAI values: the R^2 decreased to 0.26 (RMSE = 0.08 g C m^{-2} h^{-1}) and 0.32 (RMSE = 0.16 g C m^{-2} h^{-1}), respectively (Table 1). Conversely, the R^2 between SIF_{tot} and GPP showed an increasing trend as LAI increased: SIF_{tot} was also a weak predictor with R^2 = 0.27 (RMSE = 0.08 g C m^{-2} h^{-1}) for the low LAI values, confirming the negative effect of soil reflectance when the canopy was sparse, but it became a good predictor with an R^2 of 0.53 (RMSE = 0.19 g C m^{-2} h^{-1}) in the medium LAI group. Moreover, the denser canopy further enhanced the predictive advantage of SIF_{tot}: SIF_{tot} obtained a further increase in its performance in estimating GPP with R^2 = 0.57 (RMSE = 0.17 g C m^{-2} h^{-1}) when LAI was higher than 3.5 (Table 1). To remove the influence of the soil background, we only analyzed data with LAI ≥ 2.0 in the rest of this study unless otherwise explicitly stated.

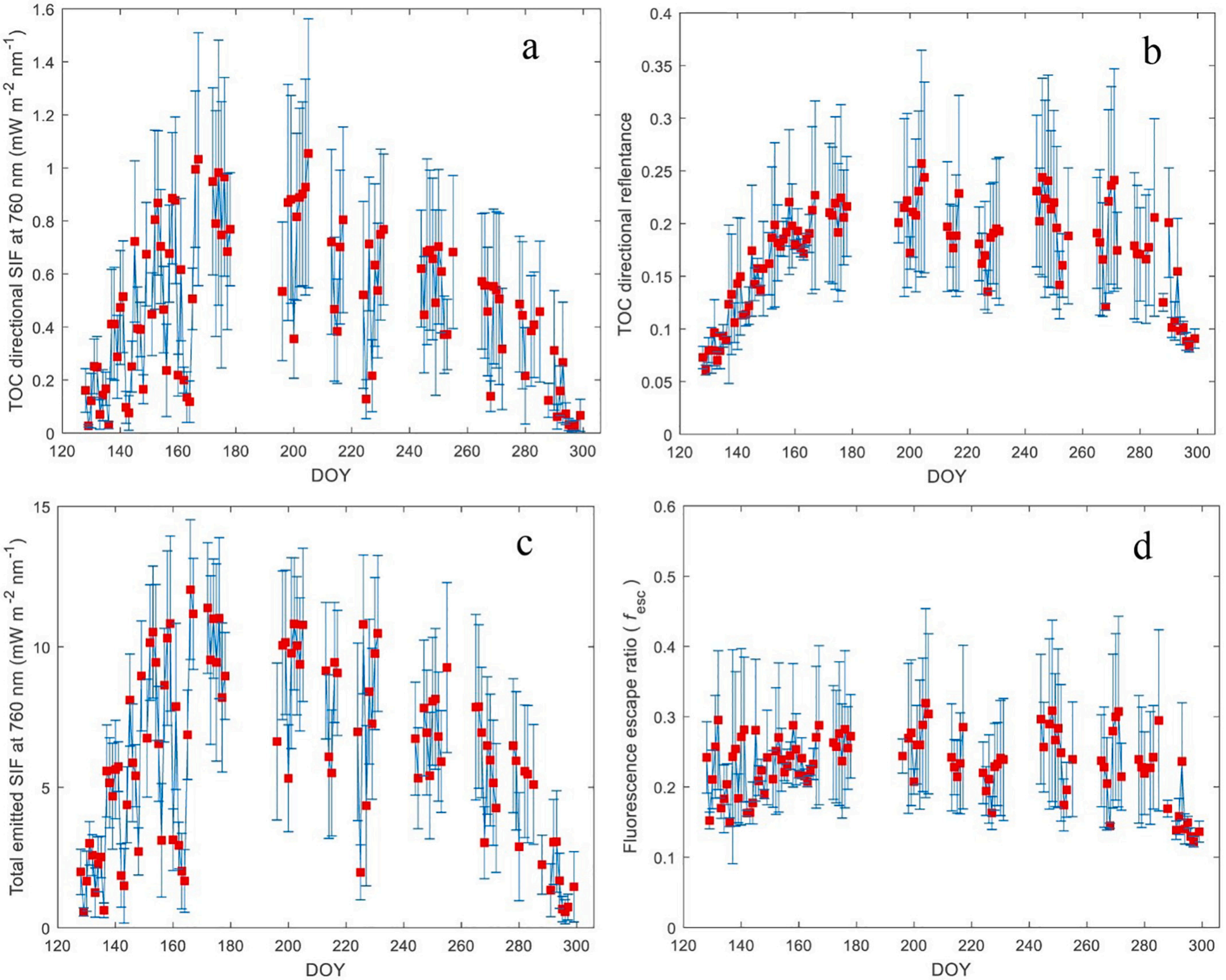

Fig. 3. The mean (the red points) and standard deviations (the error bars) of (a) top of canopy SIF emission (SIF_{toc}, mW m^{-2} sr^{-1} nm^{-1}), (b) directional reflectance (R), (c) total emitted SIF emission (SIF_{tot}, mW m^{-2} nm^{-1}) and (d) the fluorescence escape ratio (f_{esc}) to the direction of the sensor. All the four variables are for 760 nm and have a daily time step. (For interpretation of the references to colour in this figure legend, the reader is referred to the web version of this article.)

3.3. The impacts of the variations in the illumination conditions

Both GPP and SIF emission may be altered in response to the variations in the illumination conditions including the fraction of diffuse radiation and radiation saturation. Higher fraction of diffuse radiation may cause leaves in the middle and bottom canopy layers receive more solar irradiance and consequently enhance carbon sequestration by plants (Gu et al., 1999). On the other hand, an increase in diffuse fraction is typically accompanied by a decrease in both direct and total incoming irradiance (Lu et al., 2017) which likely causes a reduction in SIF emission, especially SIF_{toc}. When the *intensity* of *solar radiation* is higher than a specific threshold, both SIF and GPP may not increase with increasing irradiance level due to light saturation effect. Under this saturation condition, the variation of the SIF-GPP correlation depends on whether light stress equally affect GPP and SIF (Porcar-Castell et al., 2014). In this section, we used the fraction of diffuse PAR to assess how changes in diffuse radiation affect the predictive power of SIF_{toc} and SIF_{tot}: all data were separated by using a threshold of 0.5 in the fraction of diffuse PAR. To examine the effect of radiation saturation, we set 1300 μmol photons m^{-2} s^{-1} as the saturation point (Lu et al., 2018).

The results indicated that more diffuse radiation generally yielded the stronger SIF_{toc}-GPP and SIF_{tot}-GPP relationships. When the diffuse fraction of the radiation was higher than 0.5, the R^2 between SIF_{toc} and GPP increased by 0.10 and 0.07 in the intermediate and high LAI groups, respectively (Table 2). The predictive capability of SIF_{tot} also received the limited improvements by 0.01 and 0.08, respectively (Table 2). However, the result also showed that higher LAI values did not exaggerate the benefit of diffuse radiation in enhancing the SIF_{toc}-GPP relationship. The higher proportion of diffuse radiation led to an increase of 0.10 in the R^2 between SIF_{toc} and GPP in the medium green LAI, while it caused a smaller improvement of only 0.07 in the dense vegetation canopy (Table 2). In contrast, the benefit of higher diffuse fraction for SIF_{tot} was further enhanced in the high LAI group: its R^2 achieved the more improvement of about 0.07 than that obtained for the moderate LAI values (Table 2). Both the SIF_{toc}-GPP and SIF_{tot}-GPP relationships were deteriorated by the PAR saturation with the different magnitudes. When the PAR saturation occurred, SIF_{toc} showed the weak correlations against GPP with R^2 less than 0.20 (Table 2). The R^2 between SIF_{tot} and GPP also decreased by 0.21 and 0.27 when LAI is in the

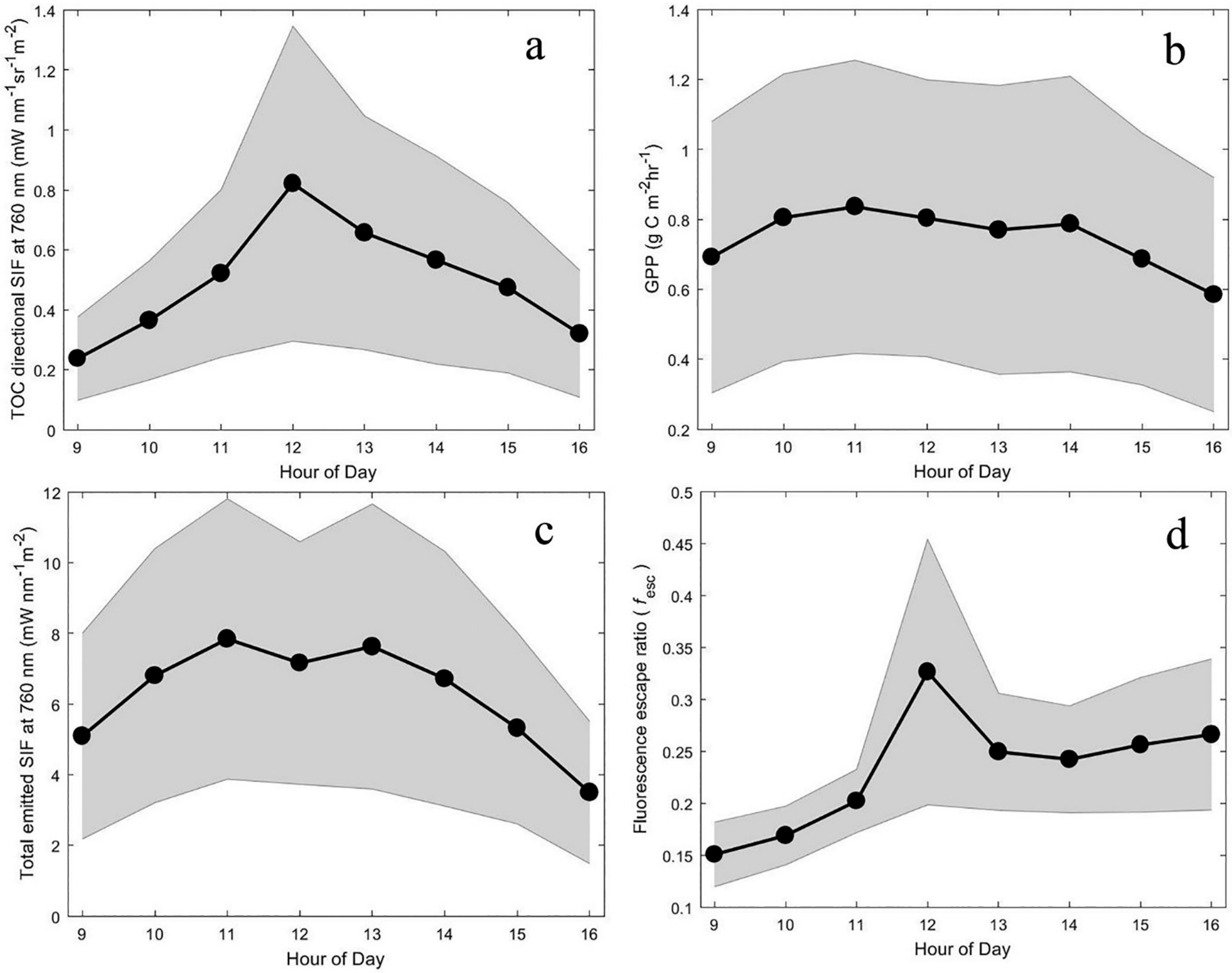

Fig. 4. The mean diurnal courses (9 a.m. to 4 p.m. local time) of (a) top of canopy SIF emission (SIF_{toc}, mW m^{-2} sr^{-1} nm^{-1}), (b) gross primary production (GPP, g C m^{-2} h^{-1}), (c) total emitted SIF emission (SIF_{tot}, mW m^{-2} nm^{-1}) and (d) the fluorescence escape ratio (f_{esc}) in the direction of the viewing direction at the Harvard Forest site in 2014. SIF_{toc}, SIF_{tot} and f_{esc} are for 760 nm. The shaded area represents the standard deviation of the mean (solid line).

intermediate and high groups (Table 2). However, SIF_{tot} demonstrated a stronger resistance to the radiation saturation: it can still predict nearly 30% of variation in GPP when PAR was higher than 1300 μmol photons m^{-2} s^{-1} (Table 2).

3.4. The impacts of the illumination geometry

In this section, we evaluated the impacts of the sun-canopy-sensor geometry on the relationship between GPP and SIF_{toc}/SIF_{tot}. Since the viewing direction of the observation system was fixed, we were unable to evaluated the impact of the view geometry and therefore we focused this study on the illumination geometry in this study.

First, we examined the influence of varying solar zenith angle (SZA, °) on the SIF_{toc}-GPP and SIF_{tot}-GPP relationships. At the study site, the daytime SZA varied in the range of 19.1°–82.5°. Because the number of measurements with high SZA was limited, we only considered data with SZA between 20°–60°. To collect sufficient data for the regression analysis, the data were binned with an increment of 4° in SZA. Overall, the R^2 of SIF_{tot}-GPP showed a generally stable trend as the solar zenith angle increased, but its values achieved the maximum of 0.63 (RMSE = 0.28 g C m^{-2} h^{-1}) when the SZA is the same to the viewing zenith angle (30° in this case) (Fig. 6). In contrast, the R^2 of SIF_{toc}-GPP showed much stronger variations at varying SZA (Fig. 6): it increased from 0.3 at a sun angle of 20° and the best predictive linear model for the GPP with R^2 of 0.55 (RMSE = 0.31 g C m^{-2} day^{-1}) was obtained at SZA = 30°. The correlation between SIF_{toc} and GPP decreased as SZA increased when SZA varied in the range of 30°-50°, but SIF_{toc} started to produce a good correspondence of GPP when SZA > 50° (Fig. 6).

Next, we particularly assessed how the hotspot effect (The shadow of the SIF tower is discussed in the supplementary information, Text S1) which describes an obvious increase in reflectance when viewing and the Sun directions coincide affected the predictive strength of SIF_{toc} and SIF_{tot}. SIF signals with sun azimuth angles between 178° - 182° (the view azimuth angle of the sensor is 180°) were assumed to be approximately located in the solar principal plane. As expected, both SIF_{toc} and SIF_{tot} had a higher R^2 with GPP as SZA approached the hotspot direction. In the exact hotspot direction (SZA = 30° in the solar principal plane), SIF_{tot} and SIF_{toc} achieved their maximal R^2 of 0.57 and 0.52 (RMSE = 0.23 and 0.25 g C m^{-2} h^{-1}), respectively (Fig. 7). In fact, the performance of SIF_{toc} in the hotspot direction was superior to that when all the daytime datasets were included (Table 1). SIF_{tot} was a better predictor for GPP than SIF_{toc} in the principal plane when SZAs

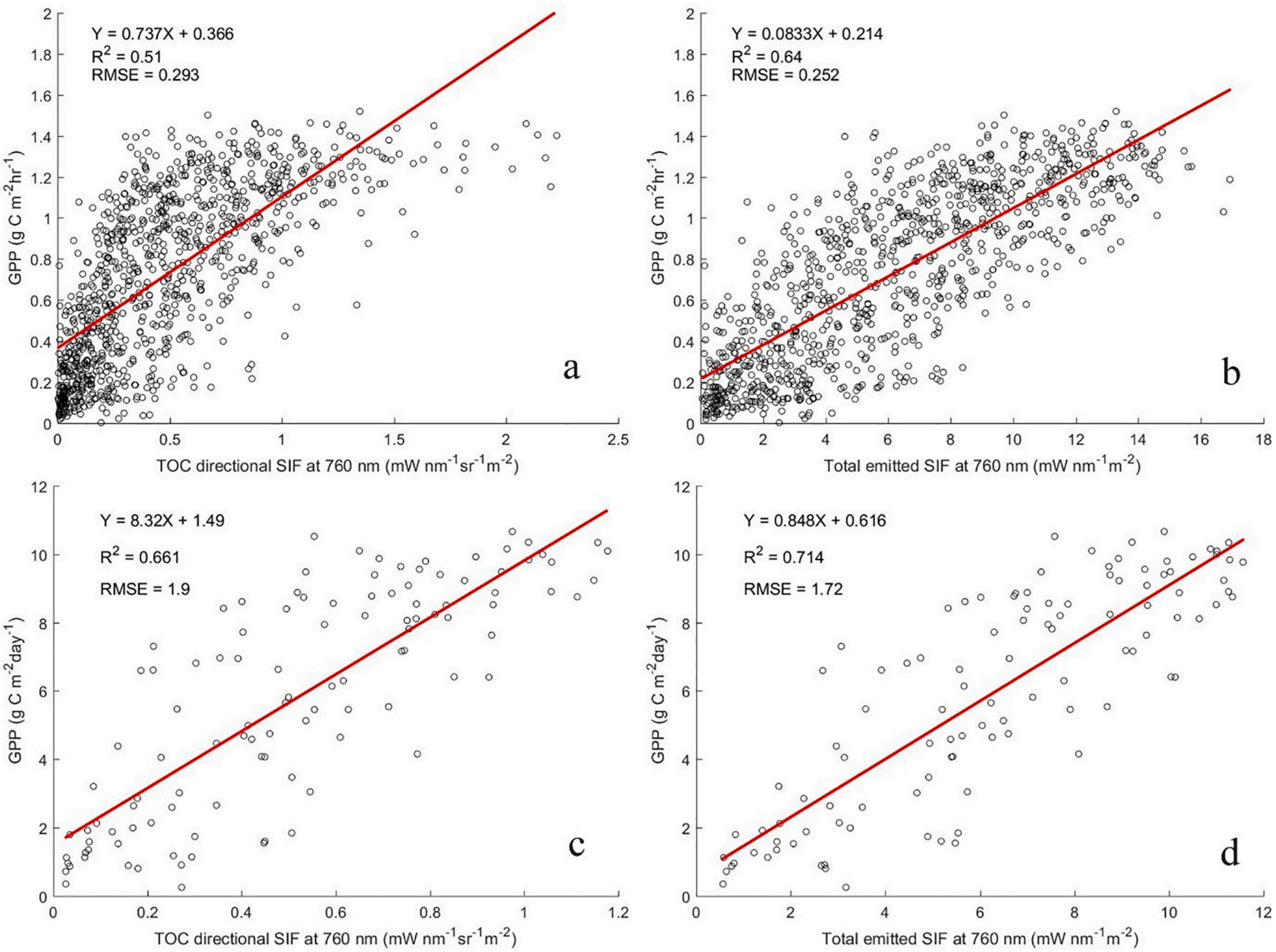

Fig. 5. The scatterplots between hourly GPP (g C m^{-2} h^{-1}) and (a) hourly SIF_{toc} (mW m^{-2} sr^{-1} nm^{-1}), (b) hourly SIF_{tot} (mW m^{-2} nm^{-1}); the scatterplots between daily GPP (g C m^{-2} day^{-1}) and (c) daily SIF_{toc} and (d) daily SIF_{tot}. The red lines are linear regression between two variables. The coefficient of determination (R^2) and root mean square error (RMSE) are also provided. (For interpretation of the references to colour in this figure legend, the reader is referred to the web version of this article.)

Table 1
The effects of leaf area index (LAI, m^2 m^{-2}) on the performance of top of canopy SIF emission at 760 nm (SIF_{toc}, mW m^{-2} sr^{-1} nm^{-1}) and total emitted SIF emission at 760 nm (SIF_{tot}, mW m^{-2} nm^{-1}) in predicting GPP (g C m^{-2} h^{-1}). All the datasets had an hourly time step and were from between 9 a.m. and 4 p.m. local time. The values are the coefficients of determination (R^2) from the linear regression analysis. The last line shows the R^2 between SIF_{toc} and SIF_{tot}.

	All	LAI ≤ 2.0	2.0 < LAI ≤ 3.5	LAI ≥ 3.5
SIF_{toc}	0.51	0.26	0.46	0.32
SIF_{tot}	0.64	0.27	0.53	0.57
(SIF_{toc}, SIF_{tot})	0.73	0.74	0.79	0.60

Table 2
The effects of the illumination conditions including fraction of diffuse radiation (f_d) and radiation saturation (Sat) on the coefficient of determination (R^2) between the hourly SIF_{toc} (mW m^{-2} sr^{-1} nm^{-1}) and SIF_{tot} (mW m^{-2} nm^{-1}) and the hourly GPP (g C m^{-2} h^{-1}) by using the linear regression analysis. All datasets belong to the period between 9 a.m. and 4 p.m. local time.

		SIF_{toc}	SIF_{tot}
2.0 < LAI ≤ 3.5	f_d ≤ 0.5	0.42	0.57
	f_d > 0.5	0.52	0.58
	No Sat	0.45	0.49
	Sat	0.12	0.28
LAI > 3.5	f_d ≤ 0.5	0.30	0.48
	f_d > 0.5	0.37	0.56
	No Sat	0.29	0.54
	Sat	0.20	0.27

varied between 20° and 50° (Fig. 7), while their performance was more comparable for the higher SZA (> 50°). Particularly, SIF_{toc} can explain almost the same variability in hourly GPP to SIF_{tot} when SZA ranged from 56° to 60° (Fig. 7).

3.5. The impacts of the meteorological variables

We examined how the meteorological variables including vapor pressure deficit (*VPD*, kPa) and air temperature (T_{air}, °C) affected the performance of SIF_{toc} and SIF_{tot} in estimating GPP. By using the median of daytime *VPD* and T_{air} as the two thresholds (0.75 kPa for *VPD*, 18.1 °C for T_{air}), all the data were divided into four groups. We found that T_{air} in 2014 had no obvious impact on the performance of SIF_{toc} and SIF_{tot} when *VPD* values were in the low group (Fig. 8). For the two

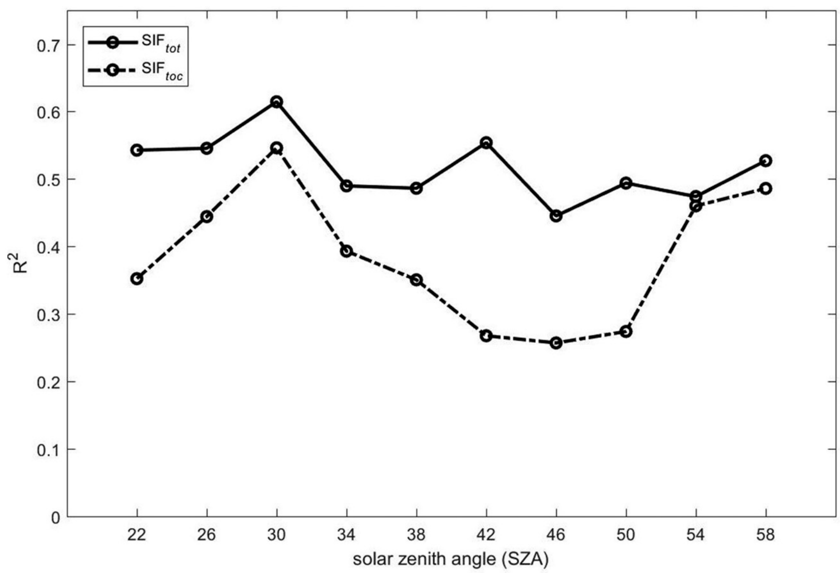

Fig. 6. The coefficients of determination (R^2) between GPP and SIF_{toc} (mW m^{-2} sr^{-1} nm^{-1}) and SIF_{tot} (mW m^{-2} nm^{-1}) as a function of solar zenith angle (SZA, °). Each point was binned every 4° of SZA. Both SIF_{toc} and SIF_{tot} are for 760 nm. All the datasets had an hourly time step and were collected during the period from 9 a.m. to 4 p.m. local time.

groups with $VPD \leq 0.75$ kPa, SIF_{tot} showed the stronger predictive strength than SIF_{toc} by explaining about 10% more variability in hourly GPP (Fig. 8). In comparison to T_{air}, VPD exerted a stronger negative influence on the link between GPP and SIF emission. The R^2 between SIF_{toc} and GPP decreased to 0.43 (RMSE = 0.27 g C m^{-2} h^{-1}) and 0.35 (RMSE = 0.30 g C m^{-2} h^{-1}) for the two groups with $VPD > 0.75$ kPa, while SIF_{tot} showed a more stable performance with R^2 of 0.61 (RMSE = 0.23 g C m^{-2} h^{-1}) and 0.54 (RMSE = 0.25 g C m^{-2} h^{-1}) for the high VPD condition (Fig. 8). Especially, SIF_{tot} owned a predictive advantage for the group with the most stressful group ($VPD > 0.75$ kPa and $T_{air} > 18.1$ °C): SIF_{tot} still accounted for 53.4% (RMSE = 0.25 g C m^{-2} h^{-1}) of GPP variability, whereas SIF_{toc} explained only 35.2% (RMSE = 0.29 g C m^{-2} h^{-1}) (Fig. 8).

4. Discussion

4.1. Soil background contamination

TOC SIF also contains the contribution of emitted SIF photons reflected by the soil. Thus, Eq. (5) is only valid for either dense canopy or black soil condition. The soil background contamination was the main reason for the poor correlations between SIF_{toc}/SIF_{tot} and GPP when the canopies were sparse (Table 1). The recent studies (Badgley et al., 2017; Zeng et al., 2019) showed that the negative impact of soil brightness can be reduced by using the NIR reflectance of vegetation which was defined as the product of NIR reflectance and the normalized difference vegetation index (NDVI). More specifically, Eq. (5) may be improved by replacing R with NDVI × R. Note that NDVI used in Eq. (5) should be acquired with the same or near sun-canopy-sensor geometry to SIF_{toc}/R. In this study, NDVI is estimated from reflectance measured by the narrowband silicon photodiode sensors also mounted on the walk-up tower (Yang et al., 2015). The performance of incorporating NDVI into SIF_{tot} ($SIF_{tot\text{-}NDVI}$) was provided in the supplementary information (Table S1). Overall, $SIF_{tot\text{-}NDVI}$ provided the moderate improvement in predicting GPP when LAI values were low. It is also worthwhile to mention that the advantage of SIF_{tot}-*NDVI* diminished with the increase in LAI values (Table S1). When LAI values were high, the incorporation of NDVI was not necessarily favorable (limited soil

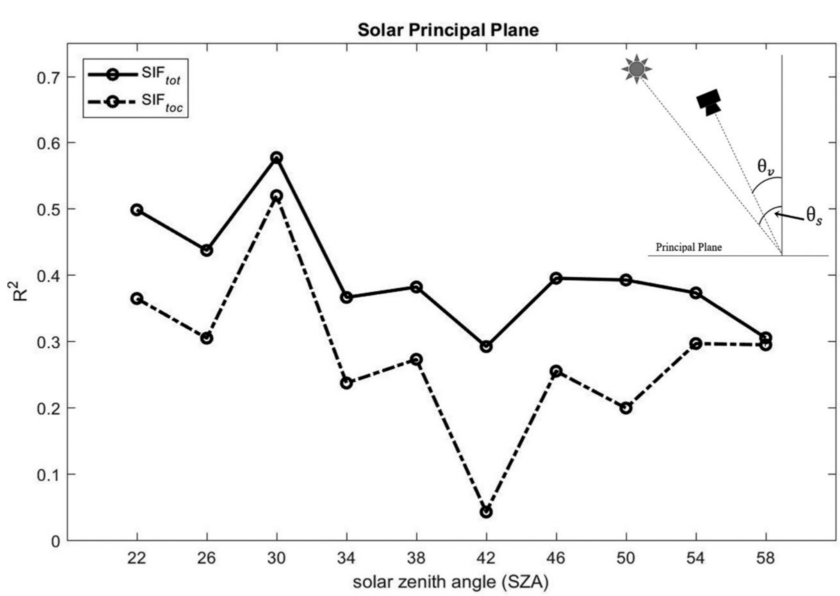

Fig. 7. The effects of solar zenith angle (SZA, °; θ_s) in the solar principal plane on the coefficients of determination (R^2) between GPP and SIF_{toc} and SIF_{tot}. SIF measurements with sun azimuth angles between 178°–182° were assumed to be approximately located in the solar principal plane. Note that the sensor was north-facing (the viewing azimuth angle of the sensor is 180°) and had the fixed viewing zenith angle (θ_v) of 30°. Each point was binned every 4° of SZA. For example, the R^2 at SZA of 30° was the mean of all R^2 values at SZA of 28–32°. These datasets have an hourly time step and were collected during the period from 9 a.m. to 4 p.m. local time.

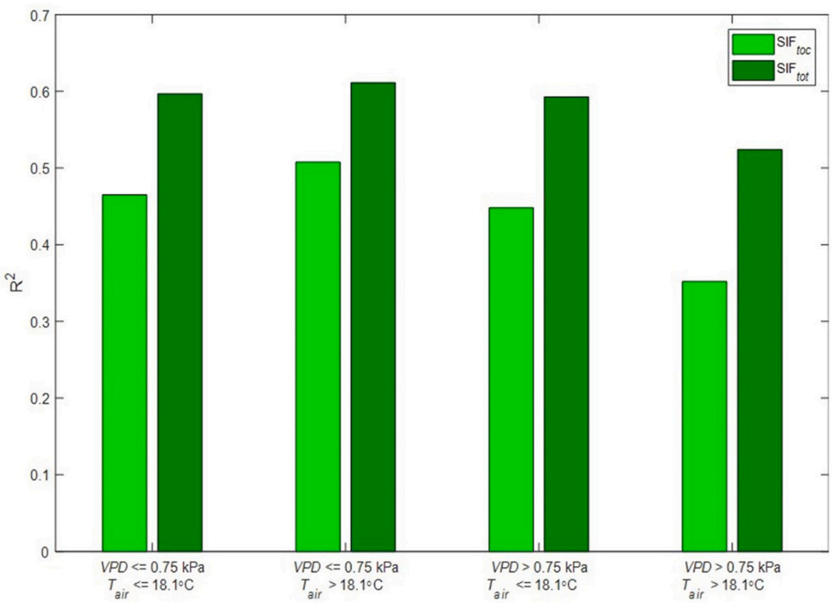

Fig. 8. The effects of vapor pressure deficit (*VPD*, kPa) and air temperature (T_{air}, °C) on the coefficients of determination (R^2) between GPP and SIF_{toc} (green, mW m^{-2} sr^{-1} nm^{-1}) and SIF_{tot} (dark green, mW m^{-2} nm^{-1}). All the datasets have an hourly time step and are from 9 a.m. to 4 p.m. local time. (For interpretation of the references to colour in this figure legend, the reader is referred to the web version of this article.)

background contamination). In turn, the negative effect of using NDVI (the different sun-canopy-sensor geometry) may deteriorate the performance of SIF_{tot}-*NDVI*. More importantly, soil background contamination was not removed in extracting SIF_{toc} from TOC radiance (Eq. (8)). Consequently, both SIF_{toc} and SIF_{tot} contained soil signals over sparse canopies, which can't be solved by incorporating NDVI. A method is needed to filter out soil signals in retrieving SIF from TOC radiance.

4.2. Variations of f_{esc}

The fact that the fluorescence escape ratio (f_{esc}) did not exhibit a seasonal variation (Fig. 3d) suggested that f_{esc} in the NIR region was largely independent of C_{ab} (Fig. S1a) and LAI (Fig. 2a). As shown in Appendix, f_{esc} is a function of ω_l and two variables related to canopy structure, namely the directional escape probability (ρ) and the recollision probability (p). As we have shown before, the response of ω_l to changing C_{ab} is very small in NIR region (Fig. 2b). At the same time, ρ and p are influenced by canopy structure and they showed the different responses (i.e. cancelling) to variations in LAI: ρ decreased with increasing LAI, but its effect on f_{esc} is compensated by an increase in p which is positively related to LAI. Although the previous study (Colombo et al., 2018) also reported that C_{dm} (Fig. S1c) had a negative effect on f_{esc} in the NIR, our results showed that its magnitude was relatively weak.

In contrast, f_{esc} demonstrated a clear diurnal pattern and it arrived its maximum in the hotspot direction (Fig. 4d), both of which supported that LAD and the sun-canopy-sensor geometry had a strong effect on f_{esc} (van der Tol et al., 2019). However, more sophisticated modelling works are needed to quantify the role of solar zenith angle, viewing direction and the different LADs in controlling f_{esc}. The fraction of sunlit leaves in view of the sensor is proportional to f_{esc}. When environmental stress is absent or weak, higher f_{esc} typically means better correlation between SIF_{toc} and GPP.

4.3. The mechanisms of the better performance of SIF_{tot}

As shown in Section 4.1, SIF_{tot} has a better performance than SIF_{toc} in mimicking the diurnal cycle of GPP. Short-term environmental stresses including strong incoming irradiance and high air temperature may occur more frequently around midday when carbon assimilation by plants is largely reduced to avoid photoinhibition and water loss. Accordingly, the diurnal patterns of GPP may exhibit the so-called midday depression of photosynthesis (Hirasawa and Hsiao, 1999; Liu et al., 2017) which explains the stable or even decreasing trend in GPP around 12 p.m. (Fig. 4b). However, NPQ does not significantly vary in response to these short-term photoinhibited circumstances (Damm et al., 2010) and in consequence, SIF_{toc} was well correlated with the diurnal variability of PAR without showing the obvious saturation phenomenon at noon (Fig. 4a, Yang et al., 2018). Their different responses to the increasing stress level at solar noon is the main reason for the weaker SIF_{toc}-GPP correlations at a diurnal basis. In comparison to SIF_{toc}, SIF_{tot} was better able to capture the diurnal pattern in GPP: the time series of hourly SIF_{tot} also contained a plateau during the period between 11 a.m. and 3 p.m. local time (Fig. 4c). The explanation is that SIF_{tot} accounted for the overall response of all the leaves to environmental stresses and only rarely was plant photosynthetic activity negatively affected by these stresses at the scale of the whole canopy. Compared to top level leaves, solar radiation received by the other lower level leaves tended to remain at a relatively low level such that SIF_{tot} unlikely had a distinct peak around noon hours. The mean diurnal course of f_{esc} also contained a peak at 12:00 p.m.: it indicated that the sensor can "see" the most of total SIF emission at noon (Fig. 4d). The observation system was north-facing, allowing measurements acquired at around noon were in or near the hotspot region, which in turn made the sensor directly see the larger illuminated area on the canopy than in other directions. Also note that low SZA at mid-day leads to a deeper penetration of radiation inside the canopy which may lead to an increase in SIF_{tot} and a correspondingly lower f_{esc}. However, our result showed that whether and to what extent illuminated area of the canopy is within the FOV of the sensor was the primary factor controlling the magnitude of f_{esc}. We also found an asymmetric pattern in the diurnal course of f_{esc}: f_{esc} was higher in the afternoon than that in the morning for the same SZAs (Fig. 4d). The similar asymmetric reflectance trajectories about solar noon may be attributed to the variations in canopy geometry due to species, planting, water stress and wind direction. Although the diurnal variation of SZA was symmetric for morning and afternoon, it did not necessarily result in the symmetry of f_{esc} on a diurnal basis (Fig. 4d). Beyond SZA, f_{esc} also depended on other factors related to the sun-sensor geometry, understory and forest scene. For example, the relative azimuth angle between sun and sensor is not symmetric over the study site for morning and afternoon.

The regression results showed that SIF_{tot} provided the more accurate GPP estimates than SIF_{toc} (Table 1). In comparison to SIF_{toc} collecting SIF signals mainly from top leaves, SIF_{tot} better represents SIF emission from all layers of the vegetation canopy. Because an increase in LAI values leads to a less contribution of background soil to TOC reflectance, the dense forest canopy tends to improve the performance of SIF_{tot} in predicting canopy GPP (Table 1). The decrease in the correlation between SIF_{toc} and SIF_{tot} under the high LAI values also confirmed that their discrepancies *became* apparent in the complex canopy structure (Table 1). Also with an increase in LAI, canopy GPP tends to have a weaker correlation with carbon uptake by top level leaves such that the advantage of SIF_{tot} should be more pronounced for the dense vegetation canopy. Similarly, an increase in the proportion of diffuse PAR makes more complete canopy participate in photosynthesis, causing leaves deeper in the canopy contribute more to the total GPP. Altogether, carbon enhancement in the mid-and lower-parts of the canopy in response to diffuse PAR is more prominent in the dense closed canopy. SIF_{toc}, however, had a weak connection with photosynthesis in the other inner leaves, which explained why its performance decreased under high LAI levels, particularly when the fraction of diffuse radiation was more than 0.50 (Table 2). It also explained why SIF_{tot} was better to capture the increase trend in GPP caused by more diffuse radiation, especially for the high LAI group (Table 2).

Compared to SIF_{tot}, the R^2 between SIF_{toc} and GPP exhibited a higher variability at changing SZAs (Fig. 6), showing the SIF_{toc}-GPP relationship was more sensitive to SZA. SZA alters not only the amount of radiation reaching vegetation canopy surfaces but also the light distribution in the canopy. Because SIF_{toc} had a limited sensitivity to the variations in SIF emission and GPP inside the canopy, a SIF_{toc}-GPP model was still *a strong function of* SZA, especially when it was developed for a forest site. The vegetation hotspot effect tended to improve the performance of both SIF_{toc} and SIF_{tot} in predicting GPP (Fig. 7). In the hotspot direction, more SIF radiance from sunlit leaves can escape and thus observed by the sensor without experiencing the scattering and absorption processes in the canopy, which explains why both SIF_{toc} and SIF_{tot} obtained these improvements. In consequence, the relationship between GPP and SIF was more closely coupled in near hotspot directions. But, it is worth noting that the hotspot effect for a north-facing sensor occurs at around noon hours. Thus, the environmental stresses caused by high air temperature and/or high *VPD* may more frequently occur at midday, which may in turn weaken the link between SIF emission and photosynthesis. However, the favorable environmental conditions in 2014 suppressed the negative impacts associated with the hotspot effect. Apart from the hotspot direction, the R^2 between SIF_{toc} and GPP showed an increase trend at high solar zenith angles ($>50^{\circ}$) (Fig. 7). Larger SZA, or a more horizontal solar beam, travels less deeply into the vegetation canopy than a more vertical solar beam. Accordingly, the importance of considering the SIF transfer process inside the canopy tended to decrease at high SZA, which diminished the difference between SIF_{toc} and SIF_{tot} (Fig. 7).

Under the adverse meteorological conditions, SIF_{tot} also produced the better correlations with GPP than using SIF_{toc} (Fig. 8). This improvement is attributed to accounting for the vertical variability of the meteorological factors within different layers of the canopy. In other words, not all the leaves in the canopy experience the same stress level represented by the above-*canopy meteorological variables. For example,* the upper leaves have a higher leaf temperature because it is more exposed to stronger light radiation. Also, higher leaf temperature and less soil water availability more likely cause top layer leaves have a higher leaf-to-air *VPD* than that in lower leaves. Thus, upper leaves may suffer higher stress level than lower canopy leaves (Damm et al., 2010). As a consequence of more stress-induced NPQ, SIF_{toc} (sensing the top of canopy) had a weaker link with GPP which was integrated from the entire vertical canopy during a period of environmental stress. The above interpretation also suggests that cautions should be taken when one uses TOC SIF datasets (e.g. SIF_{toc}) to detect the impacts of heat wave on plants (Yoshida et al., 2015). Without reflecting the response of lower canopy layers to heat stress, SIF emitted from the top of vegetation canopies may overestimate the severity of heat wave events, especially in their early stage.

4.4. Implication for developing SIF-GPP models

Although SIF_{tot} had a better performance in predicting GPP, several factors must be considered to develop a large-scale SIF-GPP model with it. To estimate SIF_{tot} from SIF_{toc}, LAI, *CI*, LAD, ω_l and f_d are needed (Eq. (5)). f_d can be estimated from cloud fraction (Gu et al., 1999); both LAI and *CI* are provided on an 8-day basis with a spatial resolution of 500 m. Previous studies (van der Tol et al., 2016; Verhoef et al., 2018) showed that TOC reflectance spectra contain important information on pigment content (e.g., chlorophyll content) and canopy structural parameters (e.g., leaf angle distribution). Leaf angle distribution has an important impact on reflectance spectra in the range of 720–1150 nm (Verrelst et al., 2015). Thus, LAD may be estimated by inversion of a *vegetation* canopy *reflectance model (*Hu et al., 2018*)*. ω_l is mainly controlled by leaf structure and a variety of leaf biochemical constituents including: C_{ab}, C_{dm} and C_w: C_{ab} can be estimated from reflectance at red bands (Dash and Curran, 2004); C_{dm} accounted for over 40% of the variability in the 770–950 nm spectral window and C_w determined more than 50% variance of reflectance between 1340 and 1390 nm (Verrelst et al., 2015). Altogether, hyperspectral reflectance between 400 and 1400 nm should be simultaneously acquired to estimate ω_l. However, it is also worthwhile to note that ω_l in the NIR region is primarily determined by leaf development phase rather than the concentrations of these constituents (Fig. 2).

Consistent to the previous studies (Kohler et al., 2018; Liu et al., 2016; Zhao et al., 2016; Yang and van der Tol, 2018), this study confirmed that SIF_{toc} had strong directional variations. One important application of satellite SIF datasets is to *upscale site*-level SIF-*GPP relationship* to regions with a regression model trained by tower-based GPP/SIF measurements (Guanter et al., 2014). Most of long-term site-level SIF measurements have a fixed observation direction, however, satellite SIF datasets are provided with different viewing geometries (the glint/target modes). It means that a SIF-GPP regression model based on SIF_{toc} may only have a good performance when remotely sensed SIF inputs have the identical or similar illumination and view geometries to those used in training this model (Zhang et al., 2018). Considering the anisotropy of the canopy SIF emission is highly similar to that of canopy reflectance (Liu et al., 2016), it is possible to correct/normalize bidirectional variation in the emitted SIF with the BRDF reflectance models. For instance, the MODIS BRDF/albedo products (Schaaf et al., 2002) may have a good potential to account for the bidirectional variation in SIF emission. Although the initial experiment showed the BRDF reflectance model successfully captured the BRDF characteristics of canopy-level SIF emission (Liu et al., 2016), more efforts should be made to quantify the impacts of direction of incoming irradiance and ratio of diffuse light (Liu et al., 2016).

The potential of SIF emission in predicting GPP may be better exploited by either downscaling to a more photosynthetically relevant level or incorporating fluorescence radiance at different wavelengths. By establishing the relationship between SIF emitted by the chloroplast and SIF measured at the canopy level with the Random Forest model, Liu et al. (2019) downscaled TOC SIF to the photosystem level. Without experiencing the absorption processes inside the leaves, SIF at the photosystem level may have a better performance in estimating GPP than SIF_{tot}. SIF emission at the photosystem level also has no directional effect such that the impact of the canopy structure and varying sun-sensor geometry is minimal. However, the RF model was trained by the dataset simulated by Soil-Canopy Observation, Photochemistry and Energy fluxes (SCOPE, Version 1.70) model (van der Tol et al., 2009). Thus, its performance was subject to uncertainties due to the model deficiencies, inaccurate parameters and unrealistic assumptions, etc., and the selection of appropriate inputs for the RF model also relied on subjective experiences. More experiments are needed to quantify the leaf internal absorptance (Porcar-Castell et al., 2014) which links SIF_{tot} to SIF at the photosystem level. The integration of red SIF or even full SIF spectrum into SIF_{tot} may provide more information for plant physiological state (Zhao et al., 2018). However, SIF emission in the red wavelengths has a much stronger absorption effect such that the method to calculate SIF_{tot} by SIF_{toc} with the recollision probability does not hold.

The variation in SIF_{toc} is affected by leaf pigment content, canopy structure, illumination condition, physiological status and viewing direction. The first three factors jointly determine the amount of radiative energy absorbed by plants and physiological status regulates the partitioning of absorbed solar energy into the three pathways including photosynthesis. Although SIF_{tot} produced a stronger correlation with GPP by incorporating the impacts of canopy structure and viewing direction, it still contained non-physiological information. Thus, it may lead to a bias to directly use SIF_{tot} as an early indicator of forest physiological condition. The previous study (Celesti et al., 2018) showed that physiological information may be extracted from SIF_{toc} with the help of TOC reflectance. Specifically, several key biogeophysical variables were retrieved by inverting the SCOPE against measurements of TOC reflectance spectra (Yang et al., 2019). After determining these variables (or in other words, discriminating the impacts of non-physiological factors), one may develop a more robust relationship between SIF_{toc} and physiological variables such as fluorescence yield. Similarly, physiologically related variations may be also extracted from SIF_{tot}, while more efforts are needed to collect sufficient training samples and to reduce the uncertainties caused by parameterization equifinality (Tang and Zhuang, 2008).

4.5. Limitation

Several important assumptions are needed to estimate SIF_{tot}: (1) reflectance from soil background is negligible such that SIF_{tot} may have a poor correlation with GPP at sparse vegetation. Therefore, SIF_{tot} tends to have a poor performance in estimating GPP in grasslands because its soil layer may have a large impact on TOC reflectance. SIF_{tot} may also have a poor performance for ecosystems with relatively low fractions of vegetation cover such as savanna. Their understory layer may have a negative impact on the similarity between the SIF emission and reflectance, (2) reflected solar radiation and SIF emission measured by a sensor in fact interacts with both green foliage and non-green material (i.e. trunks and branches). However, the spectral invariant theory only considers green foliage matter only (Knyazikhin et al., 2013). Because the contribution from trunks and branches to canopy scattering is ignored, the method may have more uncertainties for *forest* types with large trunks, and (3) the canopy is homogeneous in structure and biochemistry. For example, Eq. (5) requires all layers in the vertical canopy profile have the same optical properties. In reality, however, these properties are heterogeneous in the vertical direction, even for crops or grasslands. The assumption of the vertical homogeneity used in this study may cause large biases in TOC reflectance and fluorescence (Zhao et al., 2016).

5. Conclusion

We found that SIF_{toc} in this study only accounted for on average 22.9% of the total SIF emission. Without taking into account these effects, SIF_{toc} may have a poor performance to estimate GPP for plants with dense canopies. The approach proposed in this study is able to better exploit the potential of SIF signals by integrating total SIF emission from the whole canopy. Under the assumption that soil reflectance is negligible and leaves in the canopy have the same optical properties, SIF_{tot} can be represented as a function of four variables including SIF_{toc}, R, i and ω_l. All of them are available in most remote sensing applications: SIF_{toc} and R are obtained from concurrent measurements of irradiance/radiance; ω_l in the NIR region and i can be estimated from the *open access* datasets.

SIF_{tot} was a better predictor of GPP at the forest study site as shown in the following three aspects: (1) SIF_{tot} was more capable of reproducing the diurnal variation of GPP, especially the midday depression of photosynthesis, (2) SIF_{tot} better represented the SIF emitted from all the layers of the canopy, which made it more suitable to estimate GPP from dense vegetation and (3) SIF_{tot} captured the vertical variability of canopy photosynthesis such that the SIF_{tot}-GPP model had a stronger resilience to environmental stresses. The rationale for achieving these improvements relies on the high similarity in the bidirectional characteristics between directional reflectance and SIF signals. In other words, TOC reflectance conveys information on the scattering/(re)absorption processes of emitted SIF.

We also showed the illumination geometry have the important impact on the relationship between SIF emission and GPP. The discrepancy between SIF_{toc} and SIF_{tot} decreased as sun zenith angle increased. This decrease was associated with the less free path that photons may travel within the canopy at high sun zenith angle. We found that the hotspot effect tended to enhance the correlations between SIF emission and photosynthesis. As the solar zenith angle approached the hotspot direction, the sensor can see more directly illuminated areas of the canopy. However, more environmental stresses possibly associated with the hotspot effect may deteriorate the SIF_{toc}/SIF_{tot}-GPP relationships.

The predictive power of SIF_{tot} may be further enhanced by either integrating SIF signals emitted from other fluorescence spectral region or downscaling to the photosystem level. However, the (re)absorption effect become more pronounced in other SIF spectral region, which may cause more uncertainties in estimating SIF_{tot}. Also, more experiments are required to better quantify the scattering and (re)absorption effects occurred inside leaves. Although these works are still needed, SIF_{tot} provides a simple but effective way to build more robust SIF-GPP models, especially for ecosystems with complex canopy.

Declaration of Competing Interest

The authors declare that they have no known competing financial interests or personal relationships that could have appeared to influence the work reported in this paper.

Acknowledge

The authors would like to thank Harvard Forest for providing site and logistic support during our research. This research was supported by U. S. Department of Energy Office of Biological and Environmental Research Grant DE-SC0006951, National Science Foundation Grants DBI 959333 and AGS-1005663, and the University of Chicago and the MBL Lillie Research Innovation Award to J. Tang. F. Zhao was supported by the National Natural Science Foundation of China (No. 41771382). We acknowledge the data support from National Earth System Science Data Sharing Infrastructure, National Science & Technology Infrastructure of China (http://www.geodata.cn). Z. Liu was supported by the National Natural Science Foundation of China (Grant no. 41901293).

Appendix A

The photon–canopy multiple interactions start from the canopy *interceptance* (i): the fraction of incident solar radiation (E_i) that arrives at the top of canopy are intercepted by the leaves (Fig. A1). E_i is always composed of two components: direct sunlight (E_s) and diffuse skylight (E_d). The intercepted photons are scattered (transmitted and reflected) inside the canopy; the recollision probability (p) is the probability by which a scattered photon will interact with another foliage element again (Smolander and Stenberg, 2005). To account for the probability of the scattering event, leaf albedo (ω_l) is also needed

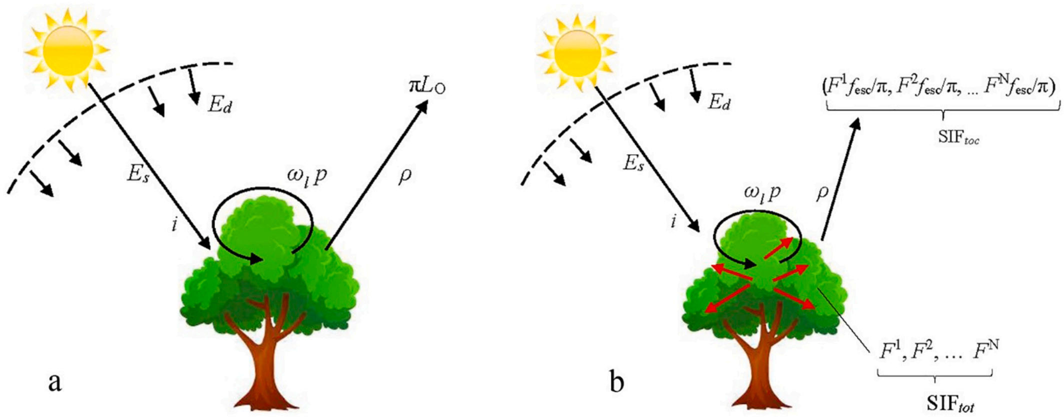

Fig. A1. The absorption and scattering processes of solar irradiance (a) and SIF emission (b) within the canopy with non-reflecting background. i is the canopy *interceptance* of incident solar irradiance (E_i), E_i is composed of direct sunlight (E_s) and diffuse skylight (E_d), p is the recollision probability, ρ is the directional escape probability, ω_l is the leaf albedo. Photons may experience a number of interactions (N) before exiting the canopy. The radiance received by the sensor (L_O) contains the contribution of photons exiting the canopy in the direction of the sensor. The fluorescent photons are excited in these scattering events with flux density of F^1, F^2..., F^N, and their summation is the total SIF emitted by all leaves (SIF_{tot}). The top-of-canopy SIF emission (SIF_{toc}) contains the contribution of fluorescent photons which escape the canopy to the sensor in the observation direction with a probability of f_{esc}.

The intercepted photons then experience one (canopy *interceptance*, no interaction again) or more scattering events (N) in the canopy and their energy can be represented as $E_i \times i \times (\omega_l)^N \times (p)^{N-1}$. The scattered photons escape the canopy and contribute to the TOC sensor with the total of πL_O (Fig. A1a). Thus, the directional escape probability (ρ) which describes a leaf within the canopy that can be viewed outside in a specific viewing direction is further needed (Huang et al., 2007; Fig. A1). In practical applications of near surface remote sensing, incoming irradiance always contains both direct sunlight (subscript "s") and diffuse skylight (subscript "d") components. R can be calculated as:

$$\left.\begin{array}{l} R = \dfrac{\pi L_O}{E_i} \\[2ex] \pi L_O = \rho_s \times (1 - f_d) \times E_i \times \sum_{k=1}^{N} i_s \times (\omega_l)^k \times p_s^{\,k-1} + \rho_d \times f_d \times E_i \times \sum_{k=1}^{N} i_d \times (\omega_l)^k \times p_d^{\,k-1} \\[2ex] R = \dfrac{\rho_s \times (1-f_d) \times E_i \times i_s \times (\omega_l + \omega_l^2 p_s + \omega_l^3 (p_s)^2 + \cdots) + \rho_d \times f_d \times E_i \times i_d \times (\omega_l + \omega_l^2 p_d + \omega_l^3 (p_d)^2 + \cdots)}{E_i} \end{array}\right\} \text{(A1)}$$

(A1)

where f_d is the fraction of diffuse solar radiation at TOC. By rearranging Eq. (A1), we obtain:

$$R = \rho_s \times (1 - f_d) \times i_s \times \frac{\omega_l}{1 - p_s \times \omega_l} + \rho_d \times f_d \times i_d \times \frac{\omega_l}{1 - p_d \times \omega_l} \tag{A2}$$

The derivation of Eqs. (A1) and (A2) requires three assumptions: (1) the contribution of soil background is negligible ('black soil'), (2) all the leaves in the canopy have the same ω_l, and (3) both ρ and p remain constant with different scattering orders.

The fluorescent photons are also excited within the canopy and experience multiple interactions. The initial fluorescence flux density excited by a total number of N photon packets can be denoted as F^1, F^2..., F^N (Fig. A1b), with the total amount of SIF_{tot}. Considering that the excited SIF photon may experience zero or more scattering orders before exiting the canopy, the fluorescence escape ratio f_{esc}, which quantifies the probability by a fluorescence photon escaping the canopy to the TOC sensor can be computed as:

$$f_{esc} = (1 - f_d) \times [\rho_s + \rho_s \omega_l p_s + \rho_s (\omega_l p_s)^2 + \rho_s (\omega_l p_s)^3 \ldots] + f_d \times [\rho_d + \rho_d \omega_l p_d + \rho_d (\omega_l p_d)^2 + \rho_d (\omega_l p_d)^3 \ldots] \tag{A3}$$

or

$$f_{esc} = (1 - f_d) \times \frac{\rho_s}{1 - p_s \times \omega_l} + f_d \times \frac{\rho_d}{1 - p_d \times \omega_l} \tag{A4}$$

By assuming that leaf emits isotropic fluorescent radiance over its abaxial or adaxial surfaces, SIF radiance received by the sensor at TOC (i.e. SIF_{toc}) can be calculated as:

$$\mathrm{SIF}_{toc} = \frac{F^1}{\pi} f_{\mathrm{esc}} + \frac{F^2}{\pi} f_{\mathrm{esc}} + \dots \frac{F^N}{\pi} f_{\mathrm{esc}}$$

$$\mathrm{SIF}_{toc} = \frac{f_{\mathrm{esc}}}{\pi} (F^1 + F^2 + \dots F^N) \tag{A5}$$

In other words, SIF_{toc} can be related to SIF_{tot} by (Fig. A2b):

$$\mathrm{SIF}_{toc} = \frac{f_{\mathrm{esc}}}{\pi} \mathrm{SIF}_{tot} \tag{A6}$$

By combining Eqs. (A2), (A4) and (A6) and assuming $p_s = p_d$ and $\rho_s = \rho_d$, one can obtain the following relationship between SIF_{toc} and SIF_{tot}:

$$\mathrm{SIF}_{tot} = \frac{\pi \times \mathrm{SIF}_{toc} \times i \times \omega_l}{R} \tag{A7}$$

Next, we used the Monte Carlo ray-tracing based Weighted Photon Spread (WPS, Zhao et al., 2016) and the method proposed by Yang et al. (2017c) model to prove that $p_s \approx p_d$ and $\rho_s \approx \rho_d$. The WPS model is a three-dimensional (3-D) radiative transfer model that used the Monte Carlo method to simulate photon transport in a plant canopy. The detailed information for the WPS simulations is summarized in Table S2. Based on empirical evidence and mathematical considerations (Goel, 1988), leaf inclination angle distributions can be described using six typical types: erectophile, planophile, spherical, uniform, plagiophile and extremophile. In this study, we considered these six types of leaf angle distributions (LADs) for five different LAI values (1, 2, 3, 4, and 5).

As we showed in supplementary information, the recollision probability of direct sunlight (p_s) is close to that (p_d) of diffuse skylight ($p_s \approx p_d$) for these six LADs under five different LAIs (1, 2, 3, 4, and 5) (Fig. S2-S6); the directional escape probability of direct sunlight (ρ_s) and diffuse skylight (ρ_d) is also close to each other ($\rho_s \approx \rho_d$) (Fig. S7-S11). At the first or two scattering orders, their difference is very small for their recollision probability (Fig. S2-S6) and directional escape probability (Fig. S7-S11), respectively. In the higher order scattering, both p and ρ remain almost constant and the *percentage of diffuse radiation has* a minimal impact on both of them (Fig. S2-S11). The simulation results show that the recollision probability and directional escape probability for direct solar irradiance is close to those for diffuse, and both of them converge their effective values when interaction order increases.

According to the method used by Yang et al. (2017c), we also computed the effective p (p_e) and effective ρ (ρ_e) with the following equations:

$$\left.\begin{aligned} p_e &= \sum\nolimits_{m=1}^{\infty} p_m w_{m-1} \\ \rho_e &= \sum\nolimits_{m=1}^{\infty} \rho_m w_{m-1} \\ w_m &= \frac{\theta_m}{\sum\nolimits_{k=0}^{\infty} \theta_k}, \text{ where } \theta_m = \sqrt[m]{p_1 p_2 \cdots p_m}, \text{ with } \theta_0 = 1. \end{aligned}\right\} \text{(A8)} \tag{A8}$$

The values of p_e and ρ_e are provided in Table S3 and Table S4 for the different leaf inclination distributions in the LAI range from 1 to 5. The comparisons for them under direct and diffusive illumination are illustrated in Fig. S12 and Fig. S13. We also calculated the coefficient of determination (R^2), the root-mean-squared error (RMSE) and the relative root-mean-square error (rRMSE, %) for p_e and ρ_e under the direct sunlight and diffuse skylight, respectively. The results (Table S5) show that p_e remains almost the same for direct light to the diffuse incoming light conditions ($R^2 > 0.99$ and rRMSE $< 1.2\%$). Also, ρ_e under direct sunlight is close to that under direct sunlight ($R^2 > 0.97$ and rRMSE $< 4.8\%$). All together, we can conclude that the corresponding p and ρ under direct and diffuse irradiance are quite close to each other: we can assume $p_s = p_d$ and $\rho_s = \rho_d$ in real applications.

Appendix B. Supplementary data

Supplementary data to this article can be found online at https://doi.org/10.1016/j.rse.2020.112083.

References

Badgley, G., Field, C.B., Berry, J.A., 2017. Canopy near-infrared reflectance and terrestrial photosynthesis. Sci. Adv. https://doi.org/10.1126/sciadv.1602244.

Celesti, M., van der Tol, C., Cogliati, S., Panigada, C., Yang, P., Pinto, F., Rascher, U., Miglietta, F., Colombo, R., Rossini, M., 2018. Exploring the physiological information of Sun-induced chlorophyll fluorescence through radiative transfer model inversion. Remote Sens. Environ. 215, 97–108. https://doi.org/10.1016/j.rse.2018.05.013.

Chen, J.M., Black, T.A., 1992. Foliage area and architecture of plant canopies from sunfleck size distributions. Agric. For. Meteorol. 60, 249–266. https://doi.org/10.1016/0168-1923(92)90040-b.

Chen, J.M., Menges, C.H., Leblanc, S.G., 2005. Global mapping of foliage clumping index using multi-angular satellite data. Remote Sens. Environ. 97, 447–457. https://doi.org/10.1016/j.rse.2005.05.003.

Colombo, R., Celesti, M., Bianchi, R., Campbell, P.K.E., Cogliati, S., Cook, B.D., Corp, L.A., Damm, A., Domec, J.C., Guanter, L., Julitta, T., Middleton, E.M., Noormets, A., Panigada, C., Pinto, F., Rascher, U., Rossini, M., Schickling, A., 2018. Variability of sun-induced chlorophyll fluorescence according to stand age-related processes in a managed loblolly pine forest. Glob. Chang. Biol. 24, 2980–2996. https://doi.org/10.1111/gcb.14097.

Damm, A., Elbers, J., Erler, A., Gioli, B., Hamdi, K., Hutjes, R., Kosvancova, M., Meroni, M., Miglietta, F., Moersch, A., Moreno, J., Schickling, A., Sonnenschein, R., Udelhoven, T., van der Linden, S., Hostert, P., Rascher, U., 2010. Remote sensing of sun-induced fluorescence to improve modeling of diurnal courses of gross primary production (GPP). Glob. Chang. Biol. 16, 171–186. https://doi.org/10.1111/j.1365-2486.2009.01908.x.

Dash, J., Curran, P.J., 2004. The MERIS terrestrial chlorophyll index. Int. J. Remote Sens. 25, 5403–5413. https://doi.org/10.1080/0143116042000274015.

Feret, J.B., Francois, C., Asner, G.P., Gitelson, A.A., Martin, R.E., Bidel, L.P.R., Ustin, S.L., le Maire, G., Jacquemoud, S., 2008. PROSPECT-4 and 5: advances in the leaf optical properties model separating photosynthetic pigments. Remote Sens. Environ. 112, 3030–3043. https://doi.org/10.1016/j.rse.2008.02.012.

Frankenberg, C., Fisher, J.B., Worden, J., Badgley, G., Saatchi, S.S., Lee, J.E., Toon, G.C., Butz, A., Jung, M., Kuze, A., Yokota, T., 2011. New global observations of the terrestrial carbon cycle from GOSAT: patterns of plant fluorescence with gross primary productivity. Geophys. Res. Lett. 38, 6. https://doi.org/10.1029/2011gl048738.

Goel, N.S., 1988. Models of vegetation canopy reflectance and their use in estimation of biophysical parameters from reflectance data. Remote Sens. Rev. 4, 1–213.

Gu, L.H., Fuentes, J.D., Shugart, H.H., Staebler, R.M., Black, T.A., 1999. Responses of net ecosystem exchanges of carbon dioxide to changes in cloudiness: results from two North American deciduous forests. J. Geophys. Res. 104, 31421–31434. https://doi.

org/10.1029/1999jd901068.
Guanter, L., Zhang, Y., Jung, M., Joiner, J., Voigt, M., Berry, J.A., Frankenberg, C., Huete, A.R., Zarco-Tejada, P., Lee, J.E., Moran, M.S., Ponce-Campos, G., Beer, C., Camps-Valls, G., Buchmann, N., Gianelle, D., Klumpp, K., Cescatti, A., Baker, J.M., Griffis, T.J., 2014. Global and time-resolved monitoring of crop photosynthesis with chlorophyll fluorescence. Proc. Natl. Acad. Sci. U. S. A. 111, E1327–E1333. https://doi.org/10.1073/pnas.1320008111.
He, L.M., Chen, J.M., Liu, J., Mo, G., Joiner, J., 2017. Angular normalization of GOME-2 Sun-induced chlorophyll fluorescence observation as a better proxy of vegetation productivity. Geophys. Res. Lett. 44, 5691–5699. https://doi.org/10.1002/2017gl073708.
Hirasawa, T., Hsiao, T.C., 1999. Some characteristics of reduced leaf photosynthesis at midday in maize growing in the field. F. Crop. Res. 62, 53–62. https://doi.org/10.1016/s0378-4290(99)00005-2.
Hu, J.C., Liu, X.J., Liu, L.Y., Guan, L.L., 2018. Evaluating the performance of the SCOPE model in simulating canopy solar-induced chlorophyll fluorescence. Remote Sens. 10. https://doi.org/10.3390/rs10020250.
Huang, D., Knyazikhin, Y., Dickinson, R.E., Rautiainen, M., Stenberg, P., Disney, M., Lewis, P., Cescatti, A., Tian, Y., Verhoef, W., Martonchik, J.V., Myneni, R.B., 2007. Canopy spectral invariants for remote sensing and model applications. Remote Sens. Environ. 106, 106–122. https://doi.org/10.1016/j.rse.2006.08.001.
Joiner, J., Yoshida, Y., Vasilkov, A.P., Yoshida, Y., Corp, L.A., Middleton, E.M., 2011. First observations of global and seasonal terrestrial chlorophyll fluorescence from space. Biogeosciences 8, 637–651. https://doi.org/10.5194/bg-8-637-2011.
Knyazikhin, Y., Schull, M.A., Stenberg, P., Mottus, M., Rautiainen, M., Yang, Y., Marshak, A., Carmona, P.L., Kaufmann, R.K., Lewis, P., Disney, M.I., Vanderbilt, V., Davis, A.B., Baret, F., Jacquemoud, S., Lyapustin, A., Myneni, R.B., 2013. Hyperspectral remote sensing of foliar nitrogen content. Proc. Natl. Acad. Sci. U. S. A. 110, E185–E192. https://doi.org/10.1073/pnas.1210196109.
Kohler, P., Guanter, L., Kobayashi, H., Walther, S., Yang, W., 2018. Assessing the potential of sun-induced fluorescence and the canopy scattering coefficient to track large-scale vegetation dynamics in Amazon forests. Remote Sens. Environ. 204, 769–785. https://doi.org/10.1016/j.rse.2017.09.025.
Leblanc, S.G., Chen, J.M., White, H.P., Latifovic, R., Lacaze, R., Roujean, J.L., 2005. Canada-wide foliage clumping index mapping from multiangular POLDER measurements. Can. J. Remote. Sens. 31, 364–376. https://doi.org/10.5589/m05-020.
Liu, L.Y., Liu, X.J., Wang, Z.H., Zhang, B., 2016. Measurement and analysis of bidirectional SIF emissions in wheat canopies. IEEE Trans. Geosci. Remote Sens. 54, 2640–2651. https://doi.org/10.1109/tgrs.2015.2504089.
Liu, L.Y., Guan, L.L., Liu, X.J., 2017. Directly estimating diurnal changes in GPP for C3 and C4 crops using far-red sun-induced chlorophyll fluorescence. Agric. For. Meteorol. 232, 1–9. https://doi.org/10.1016/j.agrformet.2016.06.014.
Liu, X., Guanter, L., Liu, L., Damm, A., Malenovský, Z., Rascher, U., Peng, D., Du, S., Gastellu-Etchegorry, J.-P., 2019. Downscaling of solar-induced chlorophyll fluorescence from canopy level to photosystem level using a random forest model. Remote Sens. Environ. 231. https://doi.org/10.1016/j.rse.2018.05.035.
Lu, X., Chen, M., Liu, Y., Miralles, D.G., Wang, F., 2017. Enhanced water use efficiency in global terrestrial ecosystems under increasing aerosol loadings. Agric. For. Meteorol. 237–238, 39–49. https://doi.org/10.1016/j.agrformet.2017.02.002.
Lu, X.L., Liu, Z.Q., An, S.Q., Miralles, D.G., Maes, W.H., Liu, Y.L., Tang, J.W., 2018. Potential of solar-induced chlorophyll fluorescence to estimate transpiration in a temperate forest. Agric. For. Meteorol. 252, 75–+. https://doi.org/10.1016/j.agrforrnet.2018.01.017.
Maignan, F., Breon, F.M., Lacaze, R., 2004. Bidirectional reflectance of Earth targets: evaluation of analytical models using a large set of spaceborne measurements with emphasis on the Hot Spot. Remote Sens. Environ. 90, 210–220. https://doi.org/10.1016/j.rse.2003.12.006.
Meroni, M., Rossini, M., Guanter, L., Alonso, L., Rascher, U., Colombo, R., Moreno, J., 2009. Remote sensing of solar-induced chlorophyll fluorescence: review of methods and applications. Remote Sens. Environ. 113, 2037–2051. https://doi.org/10.1016/j.rse.2009.05.003.
Meroni, M., Busetto, L., Colombo, R., Guanter, L., Moreno, J., Verhoef, W., 2010. Performance of Spectral Fitting Methods for vegetation fluorescence quantification. Remote Sens. Environ. 114, 363–374. https://doi.org/10.1016/j.rse.2009.09.010.
Mohammed, G.H., Colombo, R., Middleton, E.M., Rascher, U., van der Tol, C., Nedbal, L., Goulas, Y., Pérez-Priego, O., Damm, A., Meroni, M., Joiner, J., Cogliati, S., Verhoef, W., Malenovský, Z., Gastellu-Etchegorry, J.-P., Miller, J.R., Guanter, L., Moreno, J., Moya, I., Berry, J.A., Frankenberg, C., Zarco-Tejada, P.J., 2019. Remote sensing of solar-induced chlorophyll fluorescence (SIF) in vegetation: 50 years of progress. Remote Sens. Environ. 231. https://doi.org/10.1016/j.rse.2019.04.030.
Monsi, M., Saeki, T., 2005. On the factor light in plant communities and its importance for matter production. Ann. Bot. 95, 549–567. https://doi.org/10.1093/aob/mci052.
Porcar-Castell, A., Tyystjarvi, E., Atherton, J., van der Tol, C., Flexas, J., Pfundel, E.E., Moreno, J., Frankenberg, C., Berry, J.A., 2014. Linking chlorophyll a fluorescence to photosynthesis for remote sensing applications: mechanisms and challenges. J. Exp. Bot. 65, 4065–4095. https://doi.org/10.1093/jxb/eru191.
Raabe, K., Pisek, J., Sonnentag, O., Annuk, K., 2015. Variations of leaf inclination angle distribution with height over the growing season and light exposure for eight broadleaf tree species. Agric. For. Meteorol. 214–215, 2–11. https://doi.org/10.1016/j.agrformet.2015.07.008.
Schaaf, C.B., Gao, F., Strahler, A.H., Lucht, W., Li, X.W., Tsang, T., Strugnell, N.C., Zhang, X.Y., Jin, Y.F., Muller, J.P., Lewis, P., Barnsley, M., Hobson, P., Disney, M., Roberts, G., Dunderdale, M., Doll, C., d'Entremont, R.P., Hu, B.X., Liang, S.L., Privette, J.L., Roy, D., 2002. First operational BRDF, albedo nadir reflectance products from MODIS. Remote Sens. Environ. 83, 135–148. https://doi.org/10.1016/s0034-4257(02)00091-3.
Smolander, S., Stenberg, P., 2005. Simple parameterizations of the radiation budget of uniform broadleaved and coniferous canopies. Remote Sens. Environ. 94, 355–363. https://doi.org/10.1016/j.rse.2004.10.010.
Stenberg, P., 2007. Simple analytical formula for calculating average photon recollision probability in vegetation canopies. Remote Sens. Environ. 109, 221–224. https://doi.org/10.1016/j.rse.2006.12.014.
Stenberg, P., Mottus, M., Rautiainen, M., 2016. Photon recollision probability in modelling the radiation regime of canopies - a review. Remote Sens. Environ. 183, 98–108. https://doi.org/10.1016/j.rse.2016.05.013.
Tang, J.Y., Zhuang, Q.L., 2008. Equifinality in parameterization of process-based biogeochemistry models: a significant uncertainty source to the estimation of regional carbon dynamics. J. Geophys. Res. 113. https://doi.org/10.1029/2008jg000757.
van der Tol, C., Verhoef, W., Timmermans, J., Verhoef, A., Su, Z., 2009. An integrated model of soil-canopy spectral radiances, photosynthesis, fluorescence, temperature and energy balance. Biogeosciences 6, 3109–3129. https://doi.org/10.5194/bg-6-3109-2009.
van der Tol, C., Rossini, M., Cogliati, S., Verhoef, W., Colombo, R., Rascher, U., Mohammed, G., 2016. A model and measurement comparison of diurnal cycles of sun-induced chlorophyll fluorescence of crops. Remote Sens. Environ. 186, 663–677. https://doi.org/10.1016/j.rse.2016.09.021.
van der Tol, C., Vilfan, N., Dauwe, D., Cendrero-Mateo, M.P., Yang, P., 2019. The scattering and re-absorption of red and near-infrared chlorophyll fluorescence in the models Fluspect and SCOPE. Remote Sens. Environ. 232. https://doi.org/10.1016/j.rse.2019.111292.
Van Wittenberghe, S., Alonso, L., Verrelst, J., Moreno, J., Samson, R., 2015. Bidirectional sun-induced chlorophyll fluorescence emission is influenced by leaf structure and light scattering properties — a bottom-up approach. Remote Sens. Environ. 158, 169–179. https://doi.org/10.1016/j.rse.2014.11.012.
Verhoef, W., 1998. Theory of Radiative Transfer Models Applied in Optical Remote Sensing of Vegetation Canopies. Wageningen Agric. Univ https://doi.org/ISBNL 90-5485-804-4.
Verhoef, W., van der Tol, C., Middleton, E.M., 2018. Hyperspectral radiative transfer modeling to explore the combined retrieval of biophysical parameters and canopy fluorescence from FLEX - Sentinel-3 tandem mission multi-sensor data. Remote Sens. Environ. 204, 942–963. https://doi.org/10.1016/j.rse.2017.08.006.
Verrelst, J., Rivera, J.P., van der Tol, C., Magnani, F., Mohammed, G., Moreno, J., 2015. Global sensitivity analysis of the SCOPE model: what drives simulated canopy-leaving sun-induced fluorescence? Remote Sens. Environ. 166, 8–21. https://doi.org/10.1016/j.rse.2015.06.002.
Wang, W.M., Li, Z.L., Su, H.B., 2007. Comparison of leaf angle distribution functions: effects on extinction coefficient and fraction of sunlit foliage. Agric. For. Meteorol. 143, 106–122. https://doi.org/10.1016/j.agrformet.2006.12.003.
Wei, S.S., Fang, H.L., 2016. Estimation of canopy clumping index from MISR and MODIS sensors using the normalized difference hotspot and darkspot (NDHD) method: the influence of BRDF models and solar zenith angle. Remote Sens. Environ. 187, 476–491. https://doi.org/10.1016/j.rse.2016.10.039.
Yang, P.Q., van der Tol, C., 2018. Linking canopy scattering of far-red sun-induced chlorophyll fluorescence with reflectance. Remote Sens. Environ. 209, 456–467. https://doi.org/10.1016/j.rse.2018.02.029.
Yang, X., Tang, J., Mustard, J.F., Lee, J.-E., Rossini, M., Joiner, J., Munger, J.W., Kornfeld, A., Richardson, A.D., 2015. Solar-induced chlorophyll fluorescence that correlates with canopy photosynthesis on diurnal and seasonal scales in a temperate deciduous forest. Geophys. Res. Lett. 42, 2977–2987. https://doi.org/10.1002/2015gl063201.
Yang, X., Tang, J.W., Mustard, J.F., Wu, J., Zhao, K.G., Serbin, S., Lee, J.E., 2016. Seasonal variability of multiple leaf traits captured by leaf spectroscopy at two temperate deciduous forests. Remote Sens. Environ. 179, 1–12. https://doi.org/10.1016/j.rse.2016.03.026.
Yang, H., Yang, X., Zhang, Y., Heskel, M.A., Lu, X., Munger, J.W., Sun, S., Tang, J., 2017a. Chlorophyll fluorescence tracks seasonal variations of photosynthesis from leaf to canopy in a temperate forest. Glob. Chang. Biol. 23, 2874–2886. https://doi.org/10.1111/gcb.13590.
Yang, H., Yang, X., Heskel, M., Sun, S., Tang, J., 2017b. Seasonal variations of leaf and canopy properties tracked by ground-based NDVI imagery in a temperate forest. Sci. Rep. 7, 1267. https://doi.org/10.1038/s41598-017-01260-y.
Yang, B., Knyazikhin, Y., Mõttus, M., Rautiainen, M., Stenberg, P., Yan, L., Chen, C., Yan, K., Choi, S.H., Park, T.J., Myneni, R.B., 2017c. Estimation of leaf area index and its sunlit portion from DSCOVR EPIC data: algorithm theoretical basis. Remote Sens. Environ. 198, 69–84.
Yang, K., Ryu, Y., Dechant, B., Berry, J.A., Hwang, Y., Jiang, C., Kang, M., Min, J., Kimm, H., Kornfeld, A., Yang, X., 2018. Sun-induced chlorophyll fluorescence is more strongly related to absorbed light than to photosynthesis at half-hourly resolution in a rice paddy. Remote Sens. Environ. 216, 658–673. https://doi.org/10.1016/j.rse.2018.07.008.
Yang, P., van der Tol, C., Verhoef, W., Damm, A., Schickling, A., Kraska, T., Muller, O., Rascher, U., 2019. Using reflectance to explain vegetation biochemical and structural effects on sun-induced chlorophyll fluorescence. Remote Sens. Environ. 231. https://doi.org/10.1016/j.rse.2018.11.039.
Yoshida, Y., Joiner, J., Tucker, C., Berry, J., Lee, J.E., Walker, G., Reichle, R., Koster, R., Lyapustin, A., Wang, Y., 2015. The 2010 Russian drought impact on satellite measurements of solar-induced chlorophyll fluorescence: insights from modeling and comparisons with parameters derived from satellite reflectances. Remote Sens. Environ. 166, 163–177. https://doi.org/10.1016/j.rse.2015.06.008.
Zeng, Y., Badgley, G., Dechant, B., Ryu, Y., Chen, M., Berry, J.A., 2019. A practical approach for estimating the escape ratio of near-infrared solar-induced chlorophyll fluorescence. Remote Sens. Environ. https://doi.org/10.1016/j.rse.2019.05.028.
Zhang, Z.Y., Zhang, Y.G., Joiner, J., Migliavacca, M., 2018. Angle matters: bidirectional effects impact the slope of relationship between gross primary productivity and sun-induced chlorophyll fluorescence from Orbiting Carbon Observatory-2 across biomes. Glob. Chang. Biol. 24, 5017–5020. https://doi.org/10.1111/gcb.14427.
Zhao, F., Guo, Y.Q., Verhoef, W., Gu, X.F., Liu, L.Y., Yang, G.J., 2014. A method to reconstruct the solar-induced canopy fluorescence spectrum from hyperspectral measurements. Remote Sens. 6, 10171–10192. https://doi.org/10.3390/rs61010171.

Zhao, F., Li, Y., Dai, X., Verhoef, W., Guo, Y., Shang, H., Gu, X., Huang, Y., Yu, T., Huang, J., 2015. Simulated impact of sensor field of view and distance on field measurements of bidirectional reflectance factors for row crops. Remote Sens. Environ. 156, 129–142.
Zhao, F., Dai, X., Verhoef, W., Guo, Y.Q., van der Tol, C., Li, Y.G., Huang, Y.B., 2016. FluorWPS: a Monte Carlo ray-tracing model to compute sun-induced chlorophyll fluorescence of three-dimensional canopy. Remote Sens. Environ. 187, 385–399. https://doi.org/10.1016/j.rse.2016.10.036.
Zhao, F., Li, R., Verhoe, W., Cogliati, S., Liu, X.J., Huang, Y.B., Guo, Y.Q., Huang, J.X., 2018. Reconstruction of the full spectrum of solar-induced chlorophyll fluorescence: intercomparison study for a novel method. Remote Sens. Environ. 219, 233–246. https://doi.org/10.1016/j.rse.2018.10.021.